JGR Oceans

RESEARCH ARTICLE
10.1029/2021JC017848

Contrasting Sea-Ice Algae Blooms in a Changing Arctic Documented by Autonomous Drifting Buoys

Victoria Hill[1], Bonnie Light[2], Michael Steele[2], and Andrew Lowy Sybrandy[3]

[1]Department of Ocean and Earth Sciences, Old Dominion University, Norfolk, VA, USA, [2]Polar Science Center, Applied Physics Laboratory, University of Washington, Seattle, WA, USA, [3]Pacific Gyre, Oceanside, CA, USA

Key Points:

- Autonomous buoys captured the seasonal evolution of ice algae growth in first-year Arctic sea ice, bloom initiation determined by snow depth
- Early bloom onset and 70-day growth window were observed, evidence that shifts in phenology projected by climate models have occurred
- Nutrients limited ice algae growth; movement of the ice promoted turbulent diffusion of nutrients supporting high biomass

Correspondence to:
V. Hill,
vhill@odu.edu

Citation:
Hill, V., Light, B., Steele, M., & Sybrandy, A. L. (2022). Contrasting sea-ice algae blooms in a changing Arctic documented by autonomous drifting buoys. *Journal of Geophysical Research: Oceans*, *127*, e2021JC017848. https://doi.org/10.1029/2021JC017848

Received 29 JUL 2021
Accepted 1 JUL 2022

Author Contributions:
Conceptualization: Victoria Hill, Bonnie Light, Michael Steele, Andrew Lowy Sybrandy
Data curation: Victoria Hill
Formal analysis: Victoria Hill, Bonnie Light, Michael Steele
Funding acquisition: Victoria Hill, Bonnie Light, Michael Steele
Investigation: Victoria Hill, Bonnie Light, Michael Steele
Methodology: Victoria Hill, Bonnie Light, Michael Steele
Project Administration: Victoria Hill
Visualization: Victoria Hill
Writing – original draft: Victoria Hill
Writing – review & editing: Victoria Hill, Bonnie Light, Michael Steele, Andrew Lowy Sybrandy

Abstract Novel observations of the seasonal evolution of an ice algal bloom on the Chukchi shelf were collected by two autonomous buoys deployed 180 km apart in first-year drifting sea ice. High attenuation of blue light in the bottom of the ice indicated considerable accumulation of ice algae biomass with derived Chlorophyll-*a* concentrations (Chl *a*) up to 184 mg m^{-2}. Differences in the magnitude and persistence of ice algae biomass under each buoy appear to have been driven by differences in snow thickness, as ice thickness was similar between the sites. Minimal snow cover (0.02 m) around one buoy was associated with algae growth beginning in mid-May and lasting 70 days. The second buoy had notably more snow (0.4 m), causing ice algae production to lag behind the first site by approximately 4 weeks. The delay in growth diminished the peak of ice algae Chl *a* and duration compared to the first site. Light attenuation through the ice was intense enough at both buoys to have a potentially inhibiting impact on water column phytoplankton Chl *a*. Modeling ice algae growth with observed light intensities determined that nutrients were the limiting resource at the low snow site. In contrast, the algae at the high snow site were light-limited and never nutrient-limited. These data point toward changes in ice algae phenology with an earlier and longer window for growth; and nutrients rather than light determining the longevity and magnitude of production.

Plain Language Summary Ice algae growing on the underside of Arctic sea ice require light and nutrients. Light levels are enhanced beneath sea ice that is thinner and has less snow accumulation, creating a favorable environment for algal growth. This study describes results from two autonomous instrument systems installed in Arctic sea ice in March 2018. Sensors measured the amount of light transmitted through the ice and snow. Changes in the light were connected to changes in the magnitude of algae present. One site had 0.02 m of snow, and the other had 0.4 m; ice thickness was similar between the sites. Ice algae appeared in mid-May at the low-snow site, growth at the high-snow site began 4 weeks later. Numerical modeling showed that algae at the low snow site had abundant light, with growth limited by nutrients. In comparison, light was the limiting resource at the high snow site. Additionally, absorption of light by ice algae reduced the growth of water column phytoplankton under the ice. These data show that as snow cover is reduced on sea ice, ice algae could start growing earlier in the season and reach higher concentrations.

1. Introduction

There have been well-documented changes in the composition of the Arctic ice pack over the last few decades. Summertime changes are dramatic, with declines of 12.9% per decade (Kwok, 2018; Perovich et al., 2019; Stroeve & Notz, 2018). Delays in autumn freezing produce an ice pack that is dominated by thinner and more fragile first-year ice (Richter-Menge & Druckenmiller, 2020), which has also been documented to accumulate less snow, although this is variable across Arctic regions (Johnson & Eicken, 2016; Webster et al., 2018). The combination of thinner, less deformed first-year ice and a reduction in snow cover leads to earlier and increased surface ponding (Perovich & Polashenski, 2012; Polashenski et al., 2012). In addition, a trend toward earlier first spring rainfall observed since the 1990s also hastens the onset of snow melt and surface ponding (Dou et al., 2019). This overall trend of thinner ice and less snow combined with earlier snow and surface melting has a considerable impact on the timing and magnitude of the springtime increase in light transmission to the bottom of the ice and the underlying water column (Arndt & Nicolaus, 2014; Light et al., 2008, 2015; Nicolaus et al., 2012). Changes in light availability are projected to impact phenology and gross primary production (GPP) of ice algae and water column phytoplankton. Significant gains in ice algae GPP have been predicted north of 77°N driven by the replacement of the thicker multiyear ice with thinner seasonal ice, the impact south of 77°N is more uncertain as earlier light availability is counterbalanced by faster ice melt and a shortened window of production

(Lannuzel et al., 2020; Tedesco et al., 2019). Observations in the past decade have seen evidence of changes in pelagic phytoplankton phenology with large under-ice blooms observed in the spring before widescale ice retreat (Ardyna et al., 2020; Arrigo et al., 2012; Assmy et al., 2017; Hill et al., 2018; Horvat et al., 2017).

While ice algae are light-limited early in the spring when light transmission through snow and ice is low, they can still initiate colonization at intensities as low as 0.17 μmol m^{-2} s^{-1} due to their low light adaptive strategies (Hancke et al., 2018). Growth and accumulation of biomass leading to bloom conditions require irradiances over ~5 μmol m^{-2} s^{-1}, with carbon assimilation rates observed to increase as snow thins (Cota, 1985; Gosselin et al., 1986; Hancke et al., 2018; Mock & Gradinger, 1999, 2000). As ice melt progresses and melt ponds form, light increases to saturating intensities as high as 385 μmol m^{-2} s^{-1} (Gradinger, 2009; McMinn & Hegseth, 2004), and ice algae growth can become nutrient-limited (Lavoie et al., 2005; Lund-Hansen et al., 2020). Leu et al. (2015) examined existing datasets of ice algae blooms across the Arctic, growth initialized between 11 March and 10 April, and lasted approximately 60 days, placing bloom termination between 10 May and 9 June. Total biomass was variable, with the highest recorded values of ~300 mg Chl *a* m^{-2} observed within landfast ice in Resolute Bay (Leu et al., 2015). Total ice algae Chl *a* (Chlorophyll plus phaeopigments) in drifting ice on the Chukchi shelf in May and June of 2002 varied widely (0.2–304 mg m^{-2}; mean 38 mg m^{-2}), but ice floes were not revisited to track bloom development (Gradinger, 2009). Large-scale mapping of ice algae via ROVs and modeling has linked spatial heterogeneity in biomass and bloom timing primarily to snow and ice thickness (Castellani et al., 2020; Meiners et al., 2017; Melbourne-Thomas et al., 2015). However, while ice-algae blooms are *initiated* by light availability, their *persistence* is a function of nutrient supply and the timing of ice melt (Arrigo & Sullivan, 1994; Jin et al., 2006; Mortenson et al., 2017). Algae are a nutrient sink, and replenishment is necessary to support high standing stock and persistent blooms lasting one or more months (Cota et al., 1987; Thomas et al., 2010 and references therein). Nutrient replenishment generally comes from in situ regeneration, brine convection, and vertical resupply from upward fluxes, tidal action, and waves within the water column (Cota et al., 1987; Thomas et al., 2010 and references therein; Vancoppenolle et al., 2010). Future nutrient concentrations and dynamics both within the ice as well as open water remains a large uncertainty in modeling climate change impacts on Arctic marine GPP (Lannuzel et al., 2020).

While numerous different species of algae are found in Arctic sea ice, the dominant species is generally the chain-forming pennate diatom *Nitzschia frigida* Grunow, which can form a thick layer present in both the interstitial and sub-ice assemblage, protruding into the water column (Lund-Hansen et al., 2020; Michel et al., 1996; Mundy et al., 2014; Poulin et al., 2011; Syvertsen, 1991). These dense communities of ice algae absorb nearly all the radiant energy that reaches them, as they often induce active melting of the skeletal layer and sloughing of the algae, which then accelerates the demise of the bloom (Lavoie et al., 2005; Welch & Bergmann, 1989; Zeebe et al., 1996). Most importantly, dense algae blooms can inhibit water column primary production by drastically reducing light transmission through the sea ice (Mundy et al., 2007, 2014). Attenuation of photosynthetically active radiation (K_dPAR) observed in ice with large ice algae blooms has been recorded at 4 to 90 m^{-1}, over a range of Chl *a* from ~0.8 to 135 mg m^{-2}, which corresponds to less than 5% of incident light transmitted through to the water column (Ehn & Mundy, 2013; Welch & Bergmann, 1989). Ice algae also contribute to carbon export from the upper ocean to the seafloor and are linked to persistent hotspots of high macrofaunal biomass on the Chukchi shelf (Boetius et al., 2013; Feng et al., 2021; Koch et al., 2020).

Due to logistical issues involved in long-term observations on drifting sea ice, much of our understanding of ice algae bloom dynamics and its coupling with pelagic primary production comes from data collected from landfast ice. Observational technologies such as ice-tethered profilers (Laney et al., 2017) and Argo floats (Randelhoff et al., 2020), while helpful in investigating pelagic processes, are not capable of capturing ice algae development as they do not include in-ice measurements and are limited in how close to the underside of the ice they can approach. Recent under-ice mapping using ROVs (Castellani et al., 2020; Meiners et al., 2017) has provided large-scale measurements of ice algae biomass and distribution, linking these with the physical characteristics of the sea ice. However, these observations have not captured the temporal development of an ice algae bloom. Thus, there is a gap in our understanding of how ice algae blooms develop under mobile sea ice cover and how changes in sea ice thickness and light transmission impact seasonal primary production at the ice/water interface. This study presents novel observations of the seasonal development of an ice algal bloom via changes in light attenuation observed in drifting sea ice in the Chukchi Sea from two autonomous ice-tethered buoys. Observations from May through July 2018 included light intensity, temperature, and salinity in the ice and water column. A light-based productivity model was used to investigate the environmental drivers that governed the onset of ice algae growth, maximum biomass attained, and bloom duration.

Table 1
Sensors and Depths (Meters) Relative to Sea Surface at Deployment for Each Buoy

Sensor (units)		WB7 initial depth (m)	WB8 initial depth (m)
LiCor LI-192 PAR (μmol m^{-2} s^{-1})	AIR_{PAR}	0	0
	ICE_{PAR1}	0.44	0.40
	ICE_{PAR2}	0.93	0.90
	$WATER_{PAR1}$	4.93	4.90
	$WATER_{PAR2}$	9.93	9.90
	$WATER_{PAR3}$	14.93	14.90
	$WATER_{PAR4}$	19.33	19.90
	$WATER_{PAR5}$	N/A	29.90
	$WATER_{PAR6}$	N/A	48.80
In-situ Marine Optics MS9 (μW cm^{-2} nm^{-1})		4.93	4.90
Sea-Bird/Wet Labs ECO triplet fluorometer; CDOM (ppb), Backscatter 532 nm (m^{-1} sr^{-1}), *Chl a a* (mg/m^3)		5.53	5.60
Sea-Bird SBE 37-IM MicroCAT Conductivity (S/m), Salinity (PSU), Temperature (°C)		2.43, 10.53	2.41, 10.64
Sea-Bird SBE 37-IM MicroCAT Conductivity (S/m), Salinity (PSU), Temperature (°C), Pressure (decimeters)		20.42	20.90, 49.40
Temperature pods (°C)		5.13, 7.43, 12.43, 15.33	5.10, 7.40, 12.40, 15.30, 24.90, 30.25, 39.90
Camera		19.5	19.6

Note. LiCoR sensors indicate nomenclature used in the main text. "ICE" refers to a sensor frozen into the ice after deployment; "WATER" refers to a sensor in the ocean at deployment.

2. Materials and Methods

2.1. Buoy Configuration

The WArming and iRradiance Measurements (WARM) Buoy (WB) system was engineered by Pacific Gyre Inc. (Oceanside, CA, USA), consisting of a surface float supporting a suite of thermistors, conductivity sensors, irradiance sensors, and fluorometers mounted on a 20 m or 50 m long conductive cable (Table 1, Hill et al., 2018). Full configuration and data from these two systems are available at the NSF Arctic Data Center (Hill et al., 2020), and technical specifications are discussed at length in Hill et al. (2018). Here, we describe the configuration for WB7 and WB8, deployed in 2018.

Downwelling PAR (E_dPAR) incident on the sea ice (AIR_{PAR}) was recorded by a LiCor LI-192 planar irradiance sensor protruding from the top of the surface float (Figure 1). At the time of deployment, the float was lying horizontally, so the sensor only achieved a full-sky view after the float was pulled into the vertical position during ice melt. Sensors on the instrument cable were placed at varying depths (Table 1). E_dPAR within the ice and the water column was measured by six (WB7) or eight (WB8) LiCor LI-192 sensors (Table 1), and one multispectral 9-channel radiometer from In-situ Marine Optics (MS9, channels 410, 440, 490, 510, 550, 636, 660, 685, 710 nm). A Sea-Bird/Wet Labs ECO triplet fluorometer was configured to measure *Chl a* (excitation 470 nm, emission 695 nm), dissolved organic material (DOM; excitation 370 nm, emission 460 nm), and backscattering at 532 nm. The manufacturer-provided calibrations performed on 23 and 27 February (WB8 and WB7, respectively) were used to interpret the data. Sea-Bird SBE 37-IM MicroCATs provided temperature, salinity, and pressure; additional temperature pods were placed between the MicroCATs. An upward-looking OEM digital RGB camera was mounted at ~20 m depth to record images of the underside of the ice, the water column, and the buoy cable each day near solar noon. Image resolution was 120 x 160 pixels, with a full-angle field of view of 53°, imaging a ~13 × 17 m area of the underside of the ice at initial deployment, thus providing a resolution of ~0.1 m on the ice bottom. Data from all sensors were collected at hourly intervals and sent to Pacific Gyre servers via Iridium satellite.

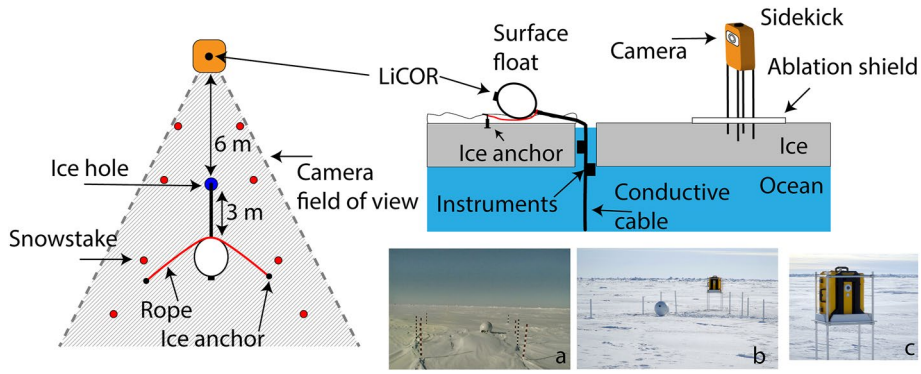

Figure 1. Plan view (left) and side view (upper right) of buoy components in the deployment configuration. (a) Sample image from sidekick camera, buoy float (WB8), red and white snow stakes are visible, (b) buoy (WB7) and sidekick after deployment, (c) close up of sidekick (WB7) with camera visible.

A separate surface unit (named "Sidekick", hereafter designated SK) provided downwelling surface irradiance (LiCor-192), air temperature, GPS position, and a daily photograph of surface conditions around the buoy (Figure 1). The SK sensors were integrated into a watertight Pelican box and mounted on a 1 m tall metal stand placed on an "ablation shield," that is, a piece of white plywood to reflect sunlight and retard snowmelt. The SKs were positively buoyant and able to send data even after the ice melted. Data and position from the SK were sent to the Pacific Gyre servers at hourly intervals using the Iridium network.

2.2. Buoy Deployment

First-year ice was chosen for the deployment site to provide observations of the entire evolution of the summer melt process. Additionally, we expect less deformed ice to show a more consistent relationship between ice and snow thickness and the under-ice light field. First-year ice is more easily accessible, comprises a large portion of the ice pack, and is likely to be the dominant ice type in the future, particularly on the Chukchi shelf, where there is significant water column productivity. An aircraft (Single Otter) from Prudhoe Bay, Alaska, was used to reach the installation sites. On 29 March 2018, WB7 was deployed at 72.3931 N and 149.60 W. The following day WB8 was deployed at 71.8391 N and 144.3120 W. The distance between buoys at deployment was 191 km (Figure 2). Large first-year ice floes were selected for the sites. Once on-site, a flat homogenous region of the floe away from existing ridges was chosen for the deployment location to reduce the possibility of additional ridging events that could damage the buoy. A 0.25 m diameter hole was drilled, ice thickness and freeboard were recorded, and average snow thickness was measured within a 5 m radius. The conductive cable with attached sensors was deployed through the hole in the ice and positioned so that the uppermost LiCOR sensor was 0.5 m below the ice surface (see Table 1 for depths adjusted to sea level). Each buoy was deployed with a 3 m offset between the surface float and the deployment hole to avoid shading the upward looking optical sensors (Figure 1) and was held in place by a rope line and ice anchors. To hasten freezing, snow and ice chips from the drilling process were pushed into the ice hole after deployment. Wooden snow stakes (0.15 m wide, 1 m in height) with red and white painted intervals (0.1 m) were placed around each buoy (Figure 1).

2.3. Calculation of Diffuse Attenuation (K_dPAR)

Diffuse attenuation (K_dPAR) was calculated using the Bouger-Lambert law and observed irradiances (E_dPAR) recorded at each LiCOR sensor (Tables 1 and 2),

$$K_d PAR = \frac{1}{z2 - z1} ln \frac{E_d PAR(z1)}{E_d PAR(z2)} \quad (1)$$

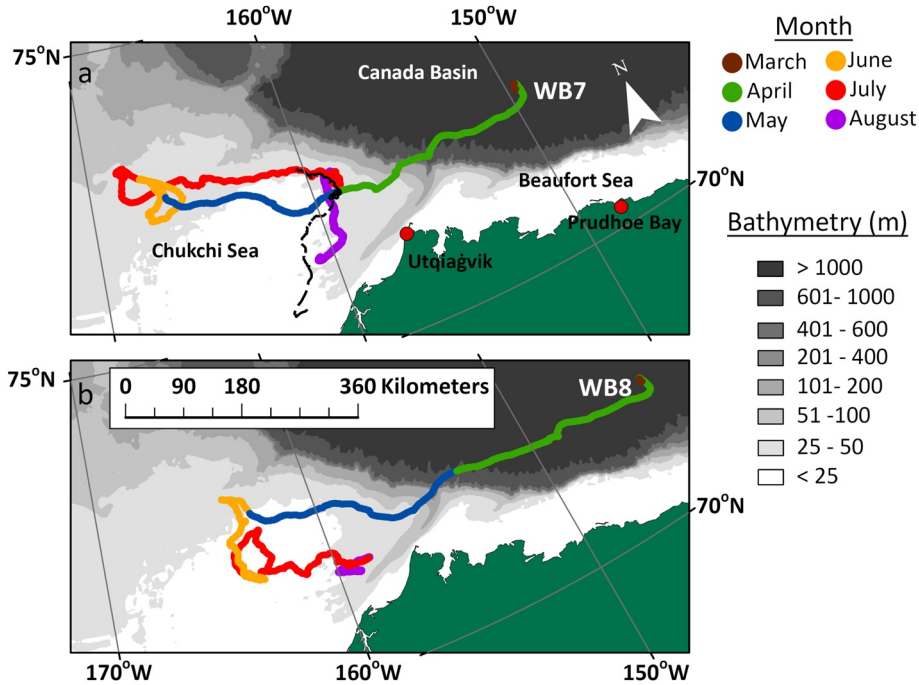

Figure 2. Map of buoy drift tracks from 2018 overlaid on NOAA bathymetry. (a) WB7, black dashed line is the location of the SK once its track diverged, (b) WB8.

where E_dPAR are the observed irradiances at geometric depths z1 and z2 (Table 1). Average daily K_dPAR was calculated from E_dPAR measured over 4 hours around solar noon (noon ± 2 hr) to avoid complications from low solar elevation angles (Hill et al., 2018). K_dPAR was calculated between adjacent sensors (Table 2) to estimate attenuation throughout the ice and water column. Negative values of K_dPAR were occasionally found, likely caused by the three dimensional light field and horizontal inhomogeneities in the ice cover. In these cases, K_dPAR values were not representative of the true attenuation properties of the ice or water column, and so were removed from the analysis.

2.4. Estimation of Chl *a*

2.4.1. Within the Ice

Previous studies in landfast ice close to Resolute Bay have presented strong relationships between the fraction of PAR irradiance transmitted through the ice algae layer (E_{trans}) and ice algae Chl *a* (Ehn & Mundy, 2013; Welch & Bergmann, 1989). The configuration of PAR sensors on the buoy allowed for similar light transmission measurements that bracketed the ice algae layer. E_{trans} was calculated between ICE_{PAR1} and ICE_{PAR2}, and ICE_{PAR2} and $WATER_{PAR1}$ sensors and then used in Equation 2 (taken from data presented in Ehn & Mundy, 2013; Welch & Bergmann, 1989) to estimate Chl *a* present within the ice algae layer over time at the buoy sites.

$$Chl\ \left(mg\,m^{-2}\right) = -61.94\,ln\,(E_{trans}) - 8.94 \quad (2)$$

Background contribution to light absorption by non-algal particles was incorporated into the original measurements and was expected to be minimal at high ice algae concentrations.

Table 2
Sensors Used to Calculate Successive K_dPAR Throughout the Ice and Water Column

Sensors	K_dPAR nomenclature
ICE_{PAR1} to ICE_{PAR2}	K_dPAR_{ICE}
ICE_{PAR2} to $WATER_{PAR1}$	$K_dPAR_{ICE/WATER}$
$WATER_{PAR1}$ to $WATER_{PAR2}$	$K_dPAR_{WATER1\_2}$
$WATER_{PAR2}$ to $WATER_{PAR3}$	$K_dPAR_{WATER2\_3}$
$WATER_{PAR3}$ to $WATER_{PAR4}$	$K_dPAR_{WATER3\_4}$

2.4.2. Within the Water Column

Chl *a* in the water column was calculated from K_dPAR at successive depths, as listed in Table 2, using a parameterization derived from data collected from the Chukchi Sea in the spring of 2014 by WB1 (Hill et al., 2016, 2018).

Contributions to K_dPAR from other absorbing compounds were assumed to be in proportion with previous studies in this area (Balch et al., 2014; Wang et al., 2005), in which non-pigmented material co-varied with Chl *a*.

$$Chl\ \left(mg\ m^{-3}\right) = 10^{3.445 * K_d PAR - 0.69} \tag{3}$$

In order to allow for comparison of ice algae Chl *a* and pelagic phytoplankton Chl *a*, volumetric Chl *a* (mg m^{-3}) was converted to water column integrated Chl *a* (mg m^{-2}) between each sensor, by multiplying Chl *a* (mg m^{-3}) retrieved by Equation 3 by the depth interval between each sensor (Table 1).

2.5. Ice Algae Growth Modeling

Potential ice algal growth based on observed light intensities was modeled to investigate limiting factors on ice algae growth.

2.5.1. Light-Driven Photosynthesis

The model architecture was modified from that used to model water column phytoplankton production in the Chukchi Sea using previous WARM buoy observations (Hill et al., 2018). Biomass-specific net photosynthesis (P^B_{net} mg C mg Chl a^{-1} h^{-1}) of ice algae was estimated using the photosynthesis-irradiance model developed by Platt et al. (1980) and previously incorporated into ice algae production models by Arrigo and Sullivan (1994) and Lange et al. (2017). Observed light intensities collected at 1 hr intervals at ICE_{PAR2} located at the ice/water interface were used to calculate biomass-specific gross photosynthesis (P^B_{gross}, Equation 4), P^B_{net} was then calculated by subtracting biomass specific respiration (R_B) from P^B_{gross} (Equation 5).

$$P^B_{gross} = P^B_E \left[1 - exp\left(\frac{-\varnothing_m \times A^*_{\varnothing}(\lambda) \times [Chl\ a] \times Ed(\lambda, t, z)}{P^B_E}\right)\right] \tag{4}$$

$$P^B_{net} = P^B_{gross} - R_B \tag{5}$$

Spectral irradiance $E_d(\lambda, t, z)$ used in Equation 4 was calculated from light intensity at ICE_{PAR2} and the spectral shape of light after transmission through the ice (Hill et al., 2018). Terms and units used in Equation 4 are described in Table 3. Values of P^B_E and initial Chl *a* were adjusted within published ranges (Hill et al., 2018; Platt et al., 1982) to achieve the best match between the model output and the ice algae Chl *a* estimated at each buoy (Table 3). $A^*_{\varnothing}(\lambda)$ was calculated from the average Chl *a* specific absorption coefficient spectra collected in the Chukchi Sea in the spring of 2002 (Hill, 2004; Hill et al., 2018).

2.5.2. Ice Algae Growth (Chl *a*)

At the end of each time step (1 hr) Redfield ratios were used to define dissolved inorganic nitrogen and phosphorus required to convert carbon generated via photosynthesis into new biomass. Concentrations in the nutrient pool were then reduced by this amount, with NH_4^+ taken up preferentially over NO_3^-. If concentrations of either nitrogen or phosphorus were insufficient to satisfy the demand based on net photosynthesis, then ice algae growth was restricted by the most limiting nutrient. Any fixed carbon that was not used for growth was kept as an internal reserve to support respiration whenever gross photosynthesis was less than respiration. Ice algae growth was

Table 3
Terms in Biomass-Specific Net Photosynthesis Model, Equation 4

Symbol	Variable	Values
P^B_E	Biomass-specific rate of light-saturated photosynthesis (mg C mg Chl a^{-1} hr^{-1})	0.5 (WB7), 0.47 (WB8)
ϕ_m	Quantum yield of photosynthesis for absorbed photons (mol C mol^{-1} photons absorbed)	0.104 (Emerson & Lewis, 1943; Laws, 1991)
$A^*_{\varnothing}(\lambda)$	Chl *a* specific absorptance (dimensionless)	Hill et al., 2018
R_B	Biomass specific respiration (mg C mg Chl a^{-1} hr^{-1})	5% of P^B_E (Forest et al., 2011)

defined in terms of Chl *a* increase, the new biomass that was supported by nutrient availability was converted to Chl *a* using molar ratio of 60:1 for carbon:Chl *a*, this value was then used in Equation 4 at the start of the next time step of the model.

2.5.3. Nutrient Replenishment

A two-layer approach was used for nutrient uptake and replenishment. Nutrient concentrations were initialized as 0.5 mmol m^{-3} of ammonia (NH_4^+), 1 mmol m^{-3} of nitrate (NO_3), and 0.5 mmol m^{-3} of phosphorous (PO_4^{-3}) taken from Codispoti et al. (2013) for the Beaufort Sea basin. At the end of each time step, a vertical flux of nutrients (F_N) into the modeled layer was calculated via a gradient transport equation,

$$F_N = K_Z \frac{\Delta N}{\Delta Z} \tag{6}$$

where K_Z is the vertical eddy diffusivity and ΔN is the difference in nutrient concentration over the vertical interval $\Delta Z = 5$ m. ΔN was calculated as the difference between nutrients at the end of each time step and concentrations in a theoretical pool of nutrients. Concentrations were set to the initial conditions (as above) while the buoy was in the Canada Basin, but increased once the buoy was on the Chukchi shelf to reflect the higher nutrient pool (Lowry et al., 2015, $NO_3^- = 8$ mmol m^{-3}, $NH_4^+ = 2$ mmol m^{-3}, and $PO_4^{-3} = 2$ mmol m^{-3}). K_z was initially set to previously measured values (0.014 m^{-2} s^{-1}; Cota et al., 1987) in the Canadian Arctic Archipelago and revised downwards until model results were close to observations. Final values used were 1.6×10^{-5} and 2.2×10^{-5} m^2 s^{-1} for WB7 and WB8, respectively, which are in line with previous values used by Arrigo and Sullivan (1994) to model nutrient replete ice algae growth in McMurdo Sound (2.3 x 10^{-5} m^2 s^{-1}), although lower than those measured under landfast ice in Resolute Passage (Lavoie et al., 2005).

2.5.4. Ice Algae Loss

A bulk loss term was used to reproduce the observed stagnation in ice algae Chl *a* accumulation and encompassed both grazing and physical release of material from the ice (due to sloughing and basal melting). Biomass loss was initiated on 28 May and 3 June for WB7 and WB8, respectively, coinciding with the rapid slowing of observed ice algae Chl *a* accumulation (see Section 3.2.2 and 3.3.2). The loss rate was adjusted until the model reproduced the observations. The final value was 90% of new growth at each time step.

3. Results

3.1. Buoy Timelines

After deployment, both buoys drifted westward, traveling from the Canada Basin to the biologically productive Chukchi Shelf, where they drifted until loss of communication in August 2018 (Figure 2). Sensor depths remained constant until significant ice melt occurred. Surface melting of the ice caused the ice anchors securing the floats to loosen; the weight of the sensor string then pulled the cable through the ice, and the floats became vertically orientated. At this time, all the sensors became deeper, for example, the ICE_{PAR1} and ICE_{PAR2} sensors dropped beneath the ice and into the ocean. The buoy was declared to be in open water once the ice melted and the surface float resided at the sea surface.

3.1.1. WARM Buoy 7—The Case of Low Snow Accumulation

At the time of deployment (29 March), ice thickness (Zi) at WB7 was 1.0 m, average snow thickness (Zs) was 0.02 m, and ice freeboard (FB) was 0.06 m (Figure 3a). Upon deployment, the uppermost LiCOR sensor (ICE_{PAR1}) was 0.44 m below the sea surface (or 0.5 m from the top of the ice), and the second sensor (ICE_{PAR2}) was 0.93 m below the sea surface, which placed it at the ice bottom. Light shading from variations in snow thickness and high light transmission through the still unfrozen deployment hole were visible in the upward looking (UL) images collected from 20 m depth (Figure 3a). SK photographs from early May confirm little to no change in snow thickness since deployment (Figure 3b). The snow stakes visible in the SK images indicate loss of snow cover throughout May and into June (Figure 3c). By 12 May, the water column had a distinct green color, which we believe indicates the presence of ice algae in the bottom of the ice (Figure 3c). The upper water column continued to appear green well into June (Figure 3c), at which time pelagic phytoplankton were also likely contributing. Ice and snow thickness are unknown at this time. The SK fell over on 9 June, likely from an unstable surface in the initial stages of melt, although no melt ponds were visible in the daily image. However, salinity stratification (not

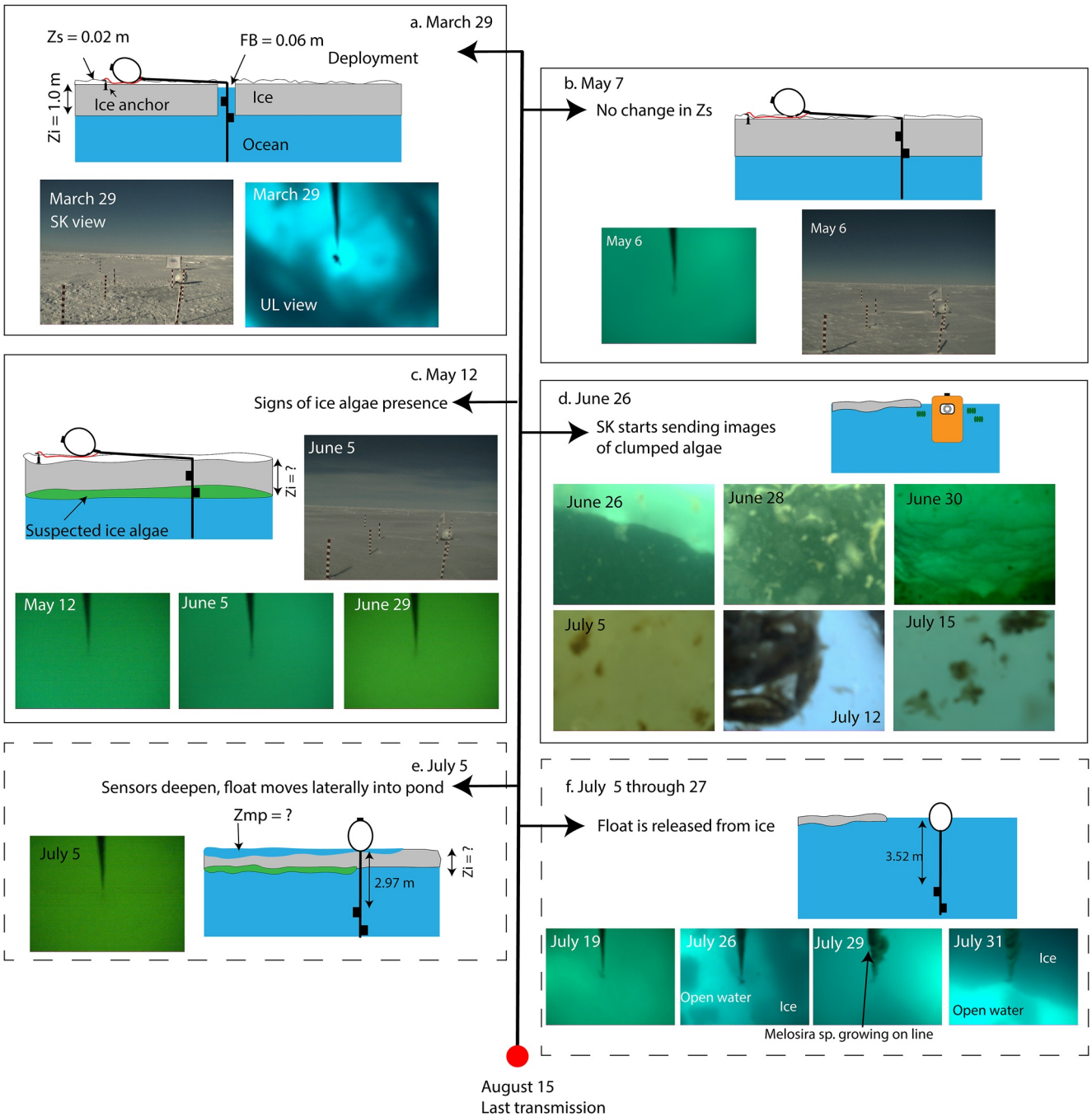

Figure 3. Timeline of events at WB7. Images are either surface view taken by the sidekick (SK view) or upwards looking (UL view) taken by the camera at 20 m depth. FB is freeboard, Zs is snow thickness, Zi is ice thickness, and Zmp is melt pond depth. Sidekick is present as in Figure 1. Continuous boxes around panels a through d indicate that the buoy was still in the deployment orientation, dashed boxes around panel e and f indicate that the buoy and sensor cable became vertically aligned.

shown) was present starting on 16 June, likely a signature of meltwater entering the ocean. On 26 June, images taken by the SK indicated that it had fallen through the ice into the ocean, where it proceeded to capture images of large clumped algae communities through mid-July (Figure 3d). In late June, the SK drifted away from WB7, reaching 1 km separation by 12 July (Figure 2a, black dashed line). The ocean pressure sensor initially located at a depth of 20.42 m (Table 1) recorded an increase in depth of 2.53 m on 5 July, caused by the melting of the ice and slippage of the cable through the ice (Figure 3e). From 5 July onwards $ICE_{PAR1\ and}$ ICE_{PAR2} were no longer in

the ice and were instead approximately 2 m or more below the underside of the ice. The persistent greenness of the water column continued after the change in sensor depths (Figure 3e). The ice gradually broke up between 5 and 27 July, at which point the buoy was floating in open water at the sea surface. Strong shading observed in the UL view at the end of July indicates remnant ice floes at the sea surface (Figure 3f). Filamentous algae grew on the instrument cable above the camera at the end of July (Figure 3f). WB7 stopped transmitting on 15 August (when its SK was 100 km away), and the SK continued to drift and collect data until November 2018.

3.1.2. WARM Buoy 8—The Case of High Snow Accumulation

Ice thickness at the WB8 deployment site was 1.08 m thick with an initial average snow thickness of 0.07 m and a freeboard of 0.10 m (Figure 4a). After deployment, the uppermost LiCOR sensor (ICE_{PAR1}) was 0.4 m from the sea surface, placing it 0.5 m from the ice surface, the second sensor (ICE_{PAR2}) was 0.9 m from the sea surface, close to the ice/water interface (~1 m from ice surface). Shading from differences in snow thickness was visible in the UL images (Figure 4a). Snow stakes visible in SK images show a ~0.40 m increase in snow thickness around the buoy between 30 March and 4 April from a storm on 31 March (Figure 4b). Drifting snow also appeared to accumulate around the buoy. Snow thickness reduced throughout May, as seen from the snow stakes. Starting at the end of May and lasting through June, the water column appeared to have a predominantly green color (Figure 4c), indicating the initial presence of ice algae followed by phytoplankton. Bare ice was visible in the SK view starting on 17 June, and on 22 June (Figure 4d), the surface float appeared to move with visible slack in the main instrument tether. We think that the ice anchors were released from the ice due to surface melt, although no change in cable sensor depths was recorded. Melt ponds were first seen on 24 June, and coverage was extensive by 29 June (Figure 4d & 4e). As in WB7, salinity stratification (not shown) was detected at WB8 starting in mid-June, likely due to this surface melt.

By 29 June, the surface float moved laterally across the ice to rest vertically in a developing melt pond (Figure 4e). The pressure sensor located at 20.9 m recorded a 2.3 m increase in depth, moving the uppermost sensor to 2.7 m below the sea surface. As melt ponds continued to develop, the SK became unstable and fell over between 6:00 and 12:00 GMT on 3 July. The last transmissions from the SK on 4 and 5 July indicate that it was floating in the ocean, where it captured the presence of large clumped algae (Figure 4f). From 3 to 19 July, the pressure sensor on the instrument tether indicated a slow increase in depth until the uppermost sensor was 3.4 m below the sea surface. We believe that the melt pond had slowly deepened until the float was released from the ice to float at the sea surface. Some strong shading captured on the UL camera could indicate nearby remnant ice (Figure 4g). The last transmission from WB8 was received on 15 August.

3.2. Low Snow Case (WB7)

3.2.1. Light Intensity

Noontime irradiance measured at both ICE_{PAR1} and ICE_{PAR2} was ~30 μmol m^{-2} s^{-1} the day after deployment and increased each day to reach 60 μmol m^{-2} s^{-1} by 11 April (Figure 5a, Table 4). At this intensity, the light was at potentially low-light adapted photosynthetically saturating rates (>16 μmol m^{-2} s^{-1}) for 10 or more hours a day. Irradiance transmitted to the ice bottom (ICE_{PAR2}) represented approximately 5% of the surface irradiance throughout April (not shown). Light reaching the bottom of the ice started to decrease around 30 April, while that at ICE_{PAR1} (0.5 m) continued to climb. Light at 0.5 m continued to exceed 60 μmol m^{-2} s^{-1}, steadily climbing to 24 hr of photosynthetically saturating light throughout June. Peak light intensity reached 500 μmol m^{-2} s^{-1} in the last week of June, far exceeding light limiting rates. Meanwhile, there was a gradual decline in the maximum light intensity at the bottom of the ice between 30 April and 30 May. By the end of May, transmission through the ice was only 1% percent of surface incident irradiance (~15 μmol m^{-2} s^{-1}). Light transmission to the bottom of the ice remained low until the end of June when melting ice caused the sensors to increase in depth by 2.5 m (see shaded area on Figure 5a).

The attenuating influence of the overlying ice heavily impacted light reaching the upper water column ($WATER_{PAR1}$, Figure 5b). Throughout April, maximum light intensities at $WATER_{PAR1}$ were approximately half that reaching the bottom of the ice (~24 μmol m^{-2} s^{-1}). Light intensity started to decrease in the last week of April, coincident with a similar pattern seen at the ice bottom (Figure 5a). On 14 May, intensities at solar noon decreased to below ~0.5 μmol m^{-2} s^{-1}, remaining so throughout May. Light intensity gradually increased throughout June, although

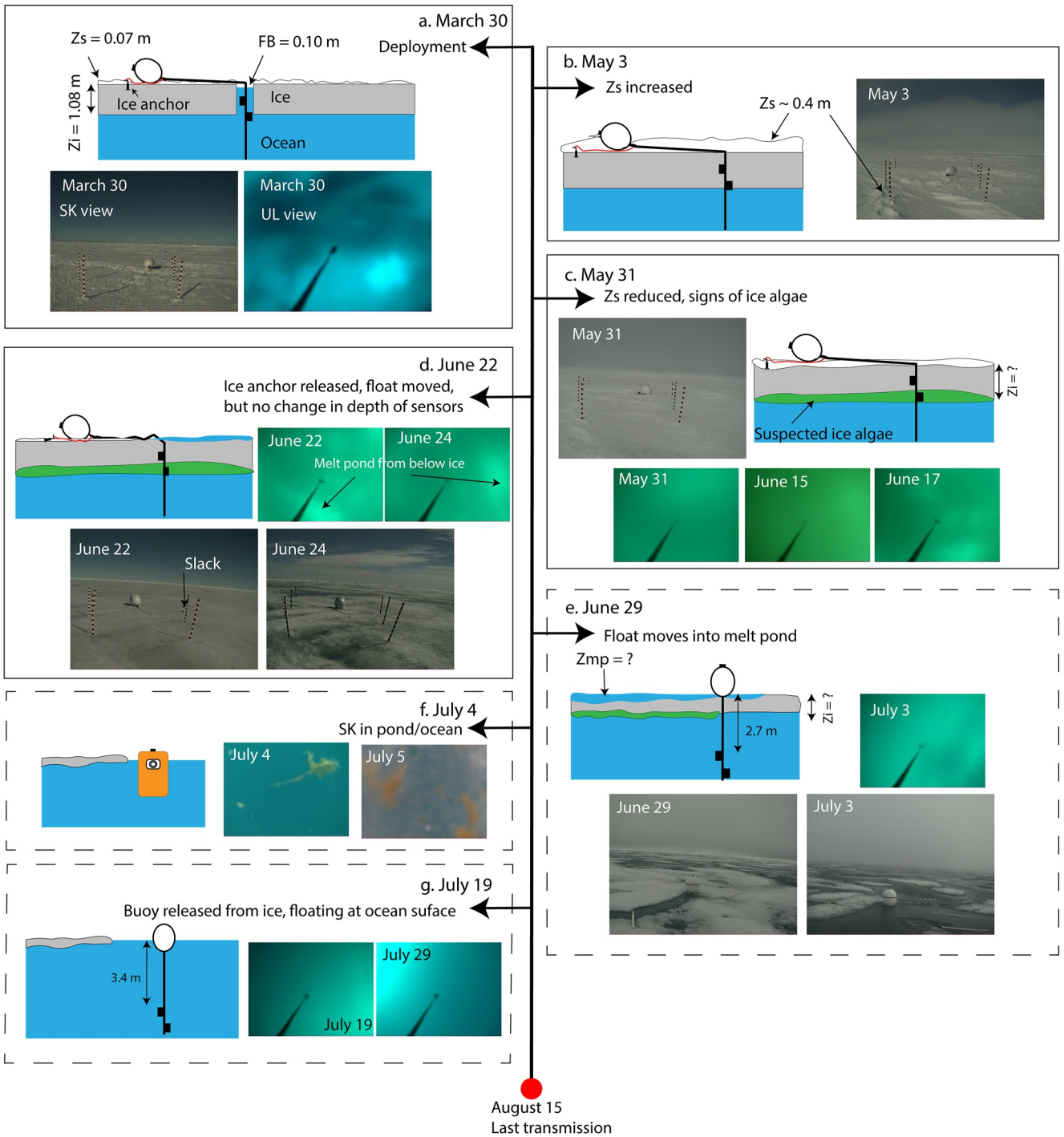

Figure 4. Timeline of events at WB8. Images are either surface view taken by the sidekick (SK view) or upwards looking (UL view) taken by the camera at 20 m. FB is freeboard, Zs is snow thickness, Zi is ice thickness. Sidekick is present as in Figure 1 but not shown. Continuous boxes around panels a through d indicate that the buoy was still in the deployment orientation, dashed boxes around panel e through g indicate that the buoy and sensor cable became vertically aligned.

values remained less than 15 μmol m^{-2} s^{-1}. A significant jump in light availability occurred as the ice melted at the start of July, and the buoy was released to float in open water.

The spectral shape of the light field provides information about the nature of the light-absorbing compounds present both in the water column and in the ice. Light in the green region of the spectrum (500–550 nm) dominated the under-ice spectra starting in April and continuing through July (Figure 5c). The decrease in blue light

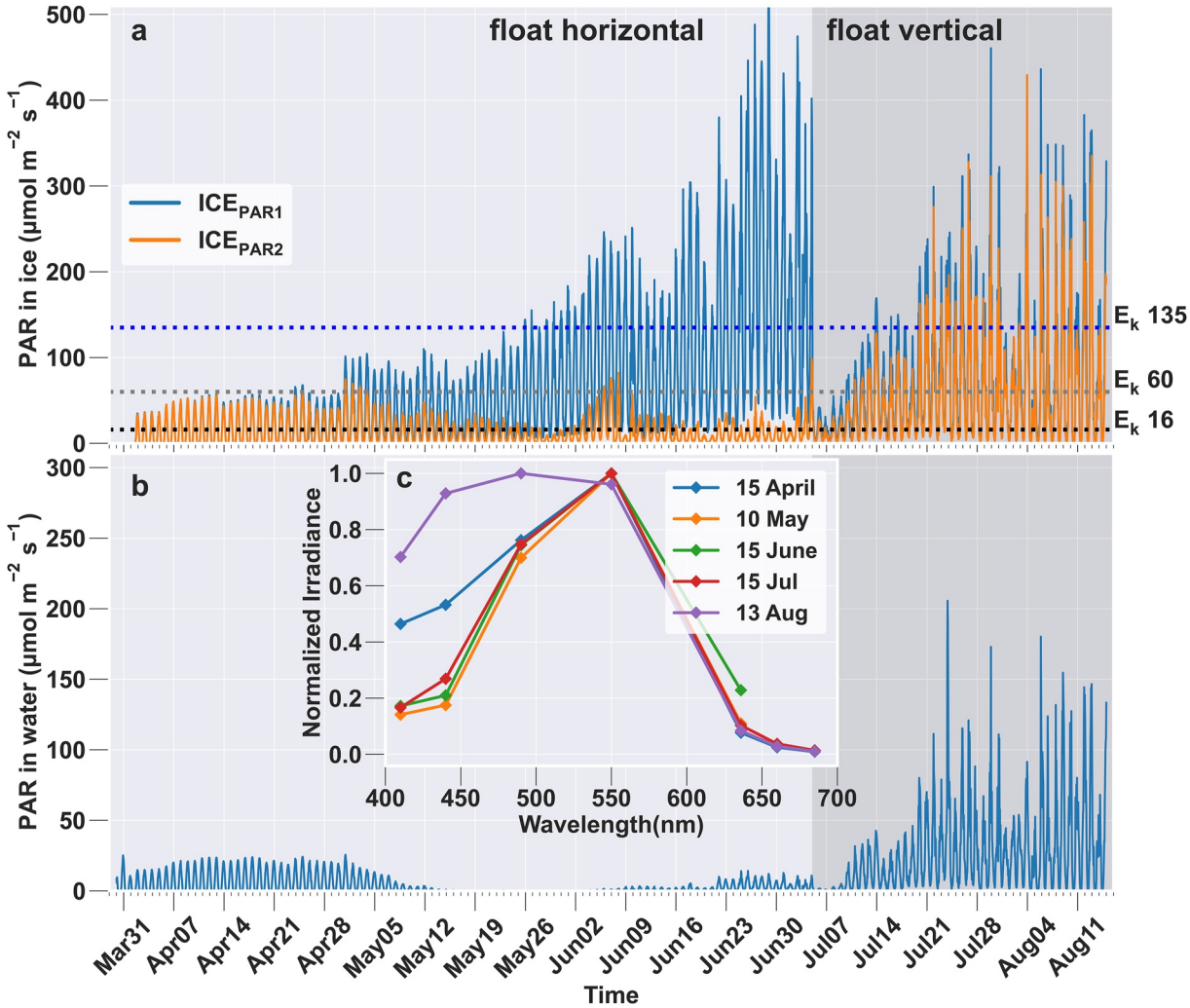

Figure 5. Observations from WB7, note the change in scale in the *y*-axis between panel a and b. (a) PAR at the ICE$_{PAR1}$ and ICE$_{PAR2}$ sensor measured at 30 min intervals. Annotated lines represent E$_k$ values (µmol m^{-2} s^{-1}) for relevant sea ice algae in the literature (Cota, 1985; Gradinger, 2009; McMinn & Hegseth, 2004). (b) PAR measured by the WATER$_{PAR1}$ sensor. (c) Example spectral profiles of light measured by the multispectral MS9 sensor (Table 1), normalized to the maximum value in each spectra. Shaded region starting 5 July represents the period of time the sensors became ~3 m deeper due to ice melt.

Table 4
Summary of Differences in Timing and Magnitude of Light Intensity and Absorption Between WB7 and WB8

Event	WB7 – low snow	WB8 - high snow
Date light at ice bottom (ICE$_{PAR2}$) reached 16 µmol m^{-2} s^{-1}	30 March	30 April
Date light at ice bottom (ICE$_{PAR2}$) reached 60 µmol m^{-2} s^{-1}	11 April	10 June
Onset of ice algae bloom. Date K_dPAR_{ICE} = 1.0 m^{-1} (equivalent Chl *a* 22 mg m^{-3})	3 May	23 May
Date and magnitude of K_dPAR_{ICE} reached at the end of the rapid increase phase. Equivalent Chl *a* in parentheses.	28 May, 5.5 m^{-1} (160 mg m^{-3})	3 June, 2.1 m^{-1} (56 mg m^{-3})
Date and magnitude of maximum Chl *a* recorded by in-water fluorometer	3 July, 8.5 mg m^{-3}	14 June, 3.2 mg m^{-3}
Duration of bloom. Date K_dPAR_{ICE} = 1.0 m^{-1}, ending when sensors dropped out of ice	63 days, 3 May – 5 July	35 days, 23 May - 27 June
Date melt ponds observed on ice surface by SK	No data	24 June

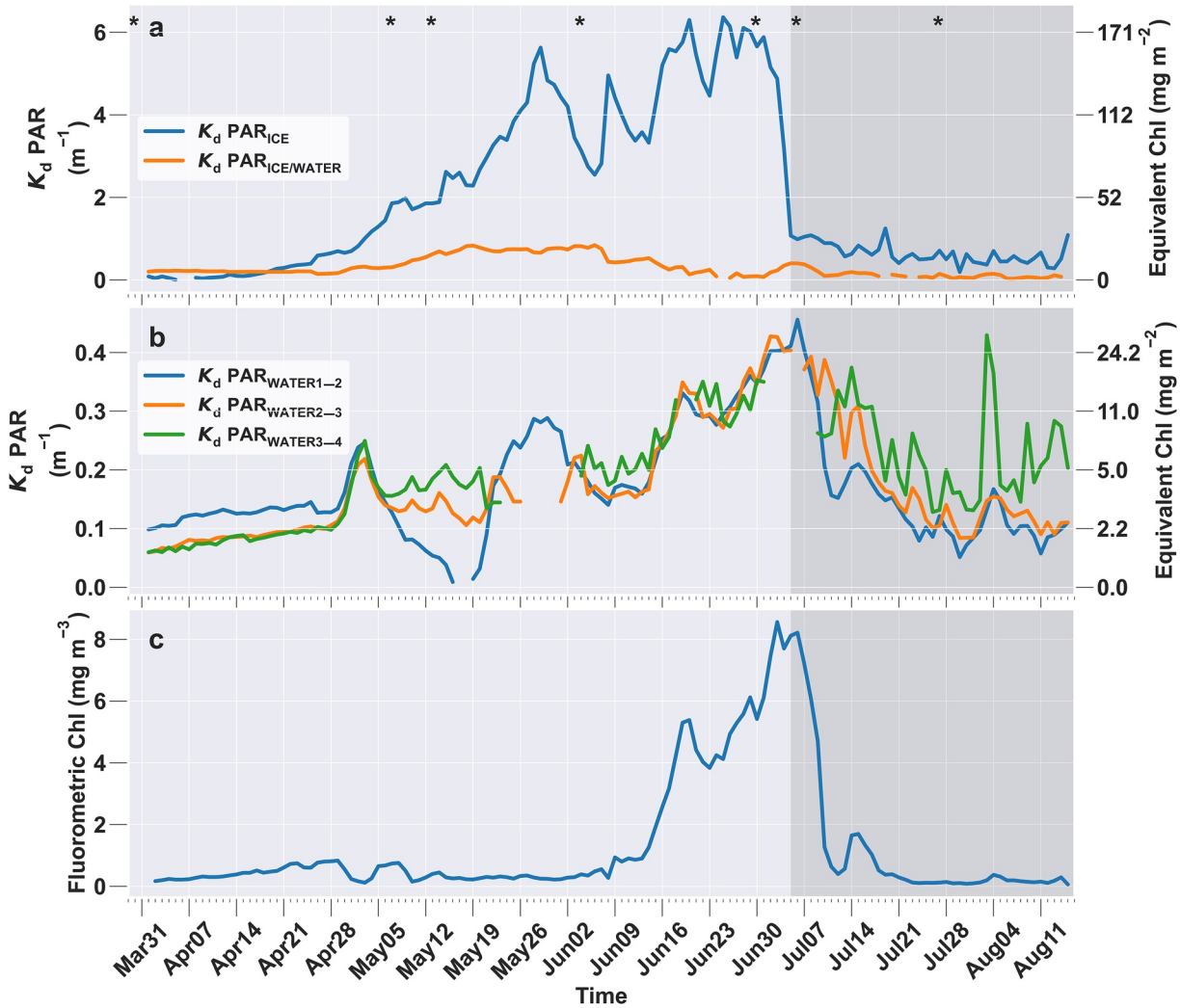

Figure 6. WB7, note the change in *Y*-axis scale between the panels (a) left axis: Diffuse attenuation in the ice; right axis: Chl *a* estimated from K_dPAR using Equation 2. (b) left axis: Diffuse attenuation in the water column; right axis: Chl *a* estimated from K_dPAR using Equation 3. (c) Chl *a* observed with ECOtriplet. Shaded region starting 5 July represents the period of time the sensors became 3 m deeper due to buoy melt out. Star symbols correspond to dates of photographs taken from the buoy shown in Figure 3.

(400–450 nm) in May, June and July is an indication of the increased presence of Chl *a* in the ice and the water column, which also coincided with the distinct green coloration observed by the underwater camera (Figure 3c). In August, an increase in the relative proportion of blue light changed the spectral shape to be more uniform across the blue/green region, also visually represented by the bluer color of the underwater pictures (Figure 3f), indicating a reduction in Chl *a* in the ice and the water column.

3.2.2. Light Attenuation and Derived Chl *a*

The diffuse attenuation within the ice (K_dPAR$_{ICE}$) was consistently low (approximately 0.2 m^{-1}) until mid-April, after which it entered a phase of rapid increase, passing 1.0 m^{-1} on 3 May (Table 4), and reaching 5.5 m^{-1} on 28 May (Figure 6a, Table 4). High values of K_dPAR$_{ICE}$ (2.2–6.1 m^{-1}) persisted throughout June, only decreasing below 1.0 m^{-1} when the sensors dropped out of the ice and into the upper water column on 5 July. During June, there were periods of high variation in K_dPAR$_{ICE}$ when values dipped by ∼1–2 m^{-1} over several days before increasing again to peak values of around 6 m^{-1}. Chl *a* estimated from light transmission varied between 70 and 184 mg m^{-2} from mid-May through June. K_dPAR between ICE$_{PAR2}$ and WATER$_{PAR1}$ (K_dPAR$_{ICE/WATER}$) captured the attenuation across the ice/water interface and any material attached to or just beneath the ice. Variation in K_dPAR$_{ICE/WATER}$ followed the same pattern of increase as K_dPAR$_{ICE}$ but at lower magnitudes. Maximum

K_dPAR$_{ICE/WATER}$ of 0.8 m^{-1} was reached in mid-May, corresponding to an approximate Chl *a* of 10 mg m^{-2}. The increase in K_dPAR$_{ICE}$ and K_dPAR$_{ICE/WATER}$ was concurrent with the observed green appearance of the water column, starting in the first week in May and continuing into July (Figure 3c), and with the attenuation of blue light within and below the ice (Figure 5c). Both K_dPAR$_{ICE}$ and K_dPAR$_{ICE/WATER}$ remained between 0.5 and 1 m^{-1} after the sensors dropped below the bottom of the ice on 5 July, indicating the continued presence of absorbing material in the upper water column.

K_dPAR within the water column (i.e., K_dPAR$_{WATER1_2}$, K_dPAR$_{WATER2_3}$, and K_dPAR$_{WATER3_4}$) was relatively homogenous with depth throughout April, May, and June (Figure 6b). K_dPAR values were <0.15 m^{-1} throughout April, increasing to around 0.2 m^{-1} in May and climbing to ~0.4 m^{-1} by the end of June. The June peak in K_dPAR represented an increase in integrated Chl *a* in the water column from ~5 to 24 mg m^{-2} over 11 days and was confirmed by data from the ECOtriplet fluorometer located at 5.53 m (Figure 6c). At its peak on 1 July, water column integrated Chl *a* in the top 20 m was ~57 mg m^{-3} and accounted for 40% of the total ice algae and phytoplankton Chl *a* present. Increased water column Chl *a* also coincided with a reduction in blue wavelengths of light observed in the upper water column (Figure 5c) and intensification of the green color of the underwater images (Figure 3c). The time-series of Chl *a* from the fluorometer (Chl a_{FL}) followed the same pattern as K_dPAR in the water column, with low Chl *a* throughout April and May increasing to ~8.5 mg m^{-3} by 3 July. In July, both K_dPAR in the water and Chl a_{FL} started to decline, linked to the sensors dropping below the ice.

3.3. High Snow Case (WB8)

3.3.1. Light Intensity

Light intensity at the high snow site was reduced compared to the low snow site. Noon light intensity at the bottom of the ice remained below 10 µmol m^{-2} s^{-1} until 25 April, roughly 6 times lower than light intensity recorded at the same time at the low snow site (Figure 7a, Table 4). Percent transmission of surface incident light to the ice bottom was <0.5% throughout April (not shown), much lower than the 5% value recorded at the low snow site. The date light intensity reached the low end of published Ek values (16 µmol m^{-2} s^{-1}; 30 April) was 30 days later than the same light intensity recorded at the low snow site. In the first week in May, the ice/water interface experienced 10 or more hours of potentially photosynthesis-saturating light (>16 µmol m^{-2} s^{-1}), a lag of 4 weeks relative to the low snow site. Light reaching the bottom of the ice started to decline around 17 May, while intensity at 0.5 m in the ice remained unchanged. Reductions in snow thickness at the start of June caused a rapid increase in light intensity at both sensors (Figure 4). Bare ice around the buoy was observed on 17 June and visible melt ponds on 24 June (Figure 4), which were associated with light intensity in the ice and ice/water interface climbing to a peak of 500 µmol m^{-2} s^{-1}, and light transmission to the ice bottom increasing to 5%. Melting of the ice resulted in the surface float being pulled into the vertical position, reducing light intensity on 27 June as all the sensors increased in depth by 2.3 m (Figures 4 and 7a).

Light in the upper water column gradually increased in magnitude throughout April and May, peaking at ~30 µmol m^{-2} s^{-1} in mid-May (Figure 7b). From mid-May through 20 June, light intensities were reduced to between 1 and 10 µmol m^{-2} s^{-1}, driven by lowered light transmission through the ice. Light intensities increased during and after ice melt, although there was high day-to-day variability. Similar to the low snow case, blue light was strongly attenuated by the overlaying ice, particularly in June (Figure 7c), indicating the presence of algae within and attached to the bottom of the ice. The removal of blue wavelengths of light, leaving green light to dominate caused the green appearance of the underwater pictures (Figure 4c). After the ice melted toward the end of July, the contribution of blue light to the underwater light field increased relative to earlier in the spring.

3.3.2. Light Attenuation and Derived Chl *a*

The attenuation of light through the bottom 0.5 m of ice (K_dPAR$_{ICE}$) increased from initially low values to reach 1.0 m^{-1} on 23 May, climbing rapidly to 2.1 m^{-1} by 2 June (Figure 8a, Table 4). This increase in light attenuation explains the reduction in light intensity observed at both the ice bottom and the upper water column. K_dPAR$_{ICE}$ stayed consistently high for 24 days until 26 June, with some small variations of ~0.3 m^{-1}. Estimated Chl *a* within the bottom of the ice throughout June varied between 50 and 60 mg m^{-2}. K_dPAR$_{ICE}$ decreased when the buoy started to melt out between 24 and 27 June, dropping the sensors below this highly attenuating layer and into the upper water column. A similar temporal pattern was present between the bottom of the ice and the upper water column sensor (K_dPAR$_{ICE/WATER}$), where attenuation increased in mid-May, reaching a high of 0.75 m^{-1} on 8 June,

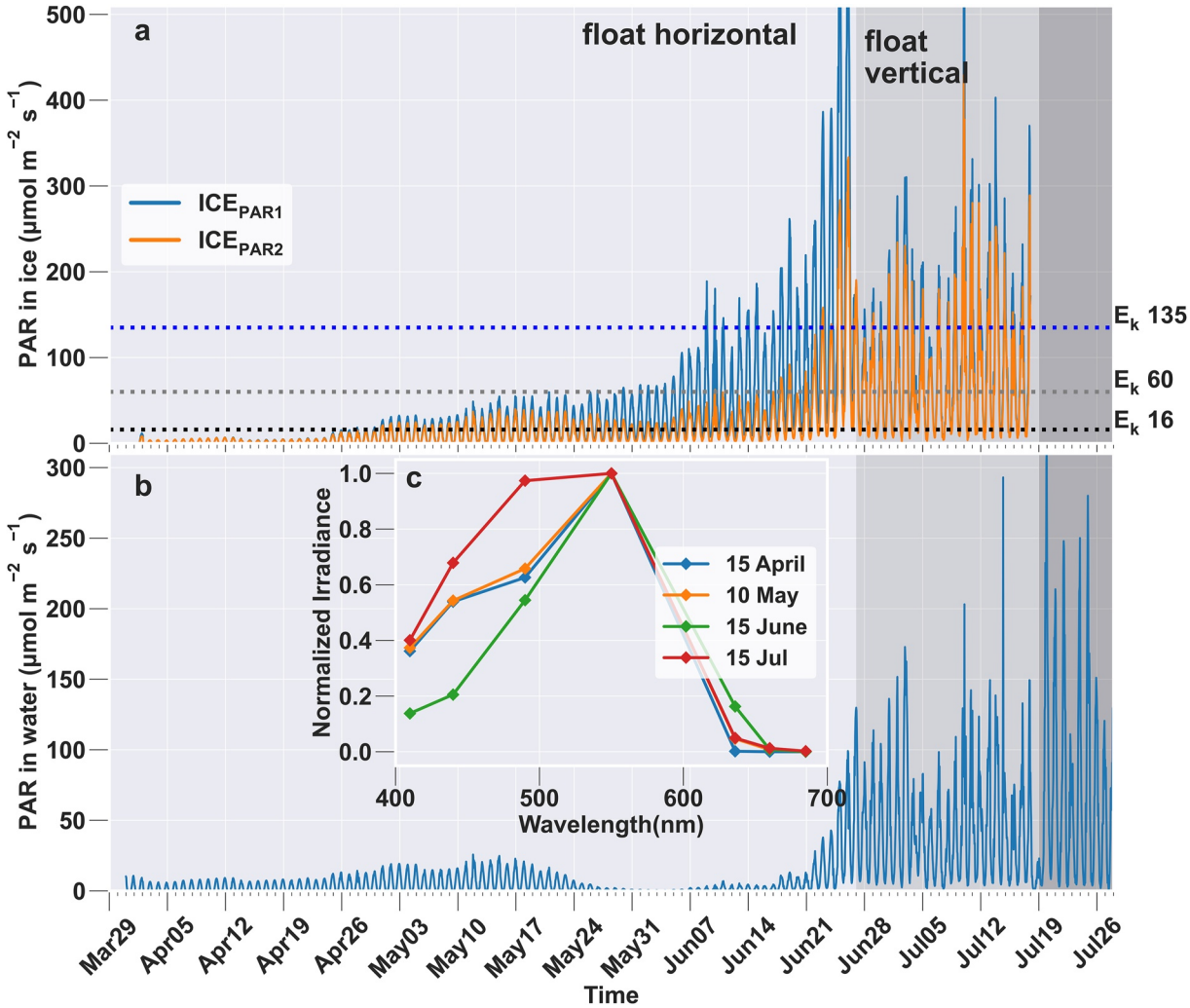

Figure 7. Observations from WB8, note the change in scale in the *y*-axis between panels a and b. (a) PAR at the ICE_{PAR1} and ICE_{PAR2} sensors measured at 30 min intervals. Annotated lines represent E_k values (µmol m^{-2} s^{-1}) for relevant sea ice algae in the literature (Cota, 1985; Gradinger, 2009; McMinn & Hegseth, 2004). (b) PAR measured by the $WATER_{PAR1}$ sensor. (c) Example spectral profiles of light measured by the MS9 sensor, normalized to the maximum value in each spectrum. Shaded regions cover the time during which the buoy gradually melted out, with the buoy dropping 1.3 m starting 27 June (first shaded area) and then another 2.5 m starting 19 July.

corresponding to Chl *a* of 4–8 mg m^{-2}. Elevated values lasted approximately 4 weeks, ending with the deepening of all sensors starting on 27 June (Figure 7a).

K_dPAR in the upper water column was homogenous throughout the deployment, with magnitudes comparable to those at the low snow site (Figure 8b). Estimated Chl *a* integrated over the upper water column was initially <4 mg m^{-2}, increasing to around 7–10 mg m^{-2} in mid May and early June. The contribution of water column Chl *a* to total Chl *a* in the system (ice plus water column) while the buoy was in the ice was <10% (May and June). Temporal variability in water column Chl *a* increased once the buoy started to melt out of the ice, with several large peaks up to ~24 mg m^{-2} observed in July. The temporal variability in water column K_dPAR was synchronous with variability in Chl a_{FL} at 4.9 m (Figure 8c), which observed several large and transient peaks in Chl *a*. The first spike in Chl a_{FL} corresponded with the reduced availability of blue light (Figure 7c) and a marked increase in the green appearance of the water (Figure 4c).

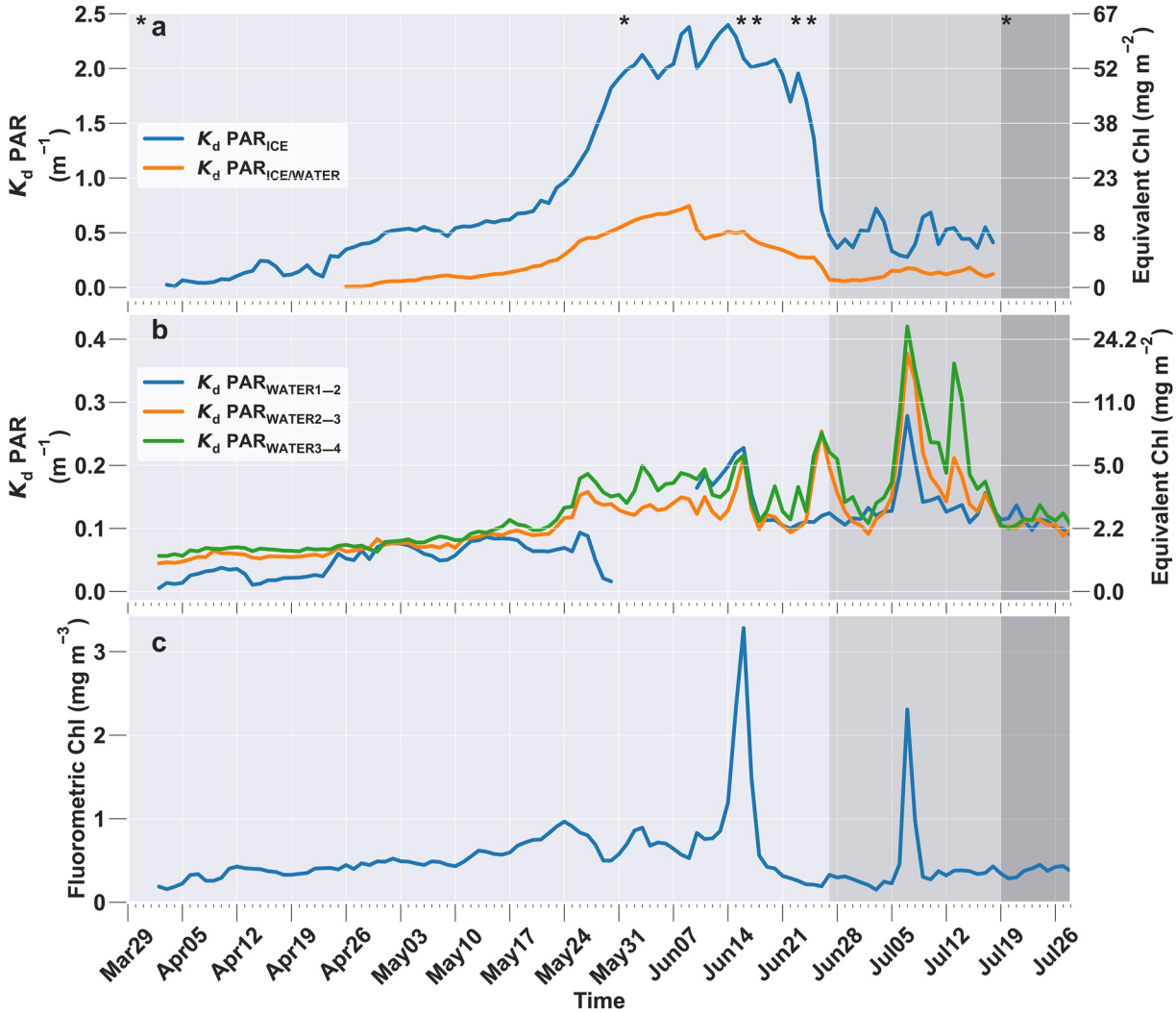

Figure 8. WB8. (a) left axis: Diffuse attenuation in the ice, right axis: Chl *a* estimated from K_dPAR using Equation 2. (b) left axis: Diffuse attenuation in the water column; right axis: estimated Chl *a* using Equation 3. (c) Chl *a* observed with ECOtriplet. Shaded regions cover the time during which the buoy gradually melted out, with the buoy dropping 1.3 m starting 27 June (first shaded area) and then another 2.5 m starting 19 July. Star symbols correspond to dates of photographs taken from the buoy shown in Figure 4.

3.4. Primary Productivity Modeling

A primary productivity model was used to help determine whether observed light intensities were sufficient to produce estimated algal densities at the bottom of the ice and to what extent other factors impacted the growth and duration of the bloom.

3.4.1. Low Snow Case (WB7)

Modeled growth rates were sensitive to changes in the biomass-specific rate of light-saturated photosynthesis (P_E^B). A 20% decrease in P_E^B reduced the algal growth rate so that the maximum modeled Chl *a* reached only 75% of estimated values. The same percentage increase in P_E^B accelerated the accumulation of biomass, so that Chl *a* was 25% higher by the end of May compared to the buoy estimations (Figure 9a).

Nutrient availability for ice algae growth, as represented in the model by vertical eddy diffusivity (K_z) and concentrations in the pool supplying the upward flux of nutrient replenishment, had significant impacts on growth rates and maximum Chl *a* reached. The larger the K_z, the more rapid the growth and the higher the predicted algal Chl *a* (Figure 9b). Differences in the impact of K_z on modeled Chl *a* are visible once growth accelerates and initial nutrients are depleted around the first week in May. A 33% increase in K_z from 1.6×10^{-5} to 2.2×10^{-5} m^2 sec^{-1}

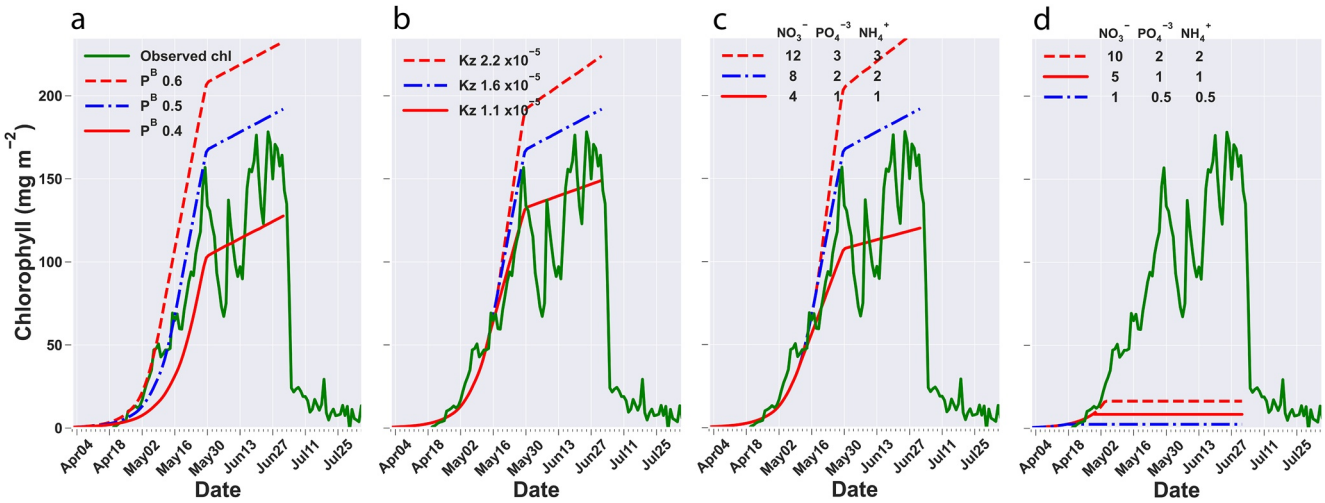

Figure 9. Sensitivity of ice algae productivity model to input variables under WB7 light conditions. Modeled Chl *a* is overlaid on estimated concentrations (green) from Figure 6 (a) biomass-specific photosynthesis rate (mg C mg Chl a^{-1} hr^{-1}), (b) K_z vertical eddy diffusivity (m^2 sec^{-1}), (c) nutrient pool concentration (mmol m^{-3}), (d) vertical diffusion off with variable initial nutrient concentration. Blue lines represent the best fit of the model output to the observations, red lines represent the impact of changing the model parameters.

resulted in a 16% increase in Chl *a* at the end of May from 166 to 192 mg m^{-3}. The predicted algae growth deviated from the initial model initialization (blue line) on 16 May, when growth was in an accelerated phase, and nutrient requirements would have been high. A decrease of 33% in K_z from 1.6×10^{-5} to 1.1×10^{-5} m^2 sec^{-1} led to a reduction in maximum Chl *a* and reduced growth from mid-May through June.

Increases in nutrient concentration in the resupply pool (i.e., in the lower layer) lead to greater upward nutrient flux, allowing for faster growth and higher Chl *a* accumulation (Figure 9c). The model sensitivity to this pool of nutrients is comparable to changes in K_z. The influence of the resupply pool concentrations did not start until the buoy drifted onto the Chukchi shelf (15 April), moving from the oligotrophic basin to the nutrient-replete shelf. A decrease in the pool of nutrients by 50% slowed growth and ultimately reduced the maximum predicted algal Chl *a* at the end of May by 19%–106 mg m^{-2}. However, if diffusion was turned off, the initial nutrient concentration controlled the timing of nutrient-limited growth (Figure 9d). Initial nutrient concentrations at expected basin levels caused nutrient limitation to occur on 17 April, while this limitation was delayed to 28 April (initial $NO_3^- = 5$ mmol m^{-3}) and 4 May (initial $NO_3^- = 10$ mmol m^{-3}) when concentrations were increased (Figure 9d).

3.4.2. High Snow Case (WB8)

Compared to the low snow case, changes in P_E^B had a larger impact on modeled growth at this site (Figure 10a). An increase or a decrease in P_E^B impacted the Chl *a* reached by June by ±50%. Controls on nutrient availability in the model parameterized through either K_z or the resupply pool did not influence ice algae growth until June (Figure 10a & 10c). After 2 June, reductions in K_z and lower layer nutrients caused the model to predict lower Chl *a*, but there was no additional growth when increasing K_z. Differences in nutrients were most influential when diffusion was zero, in which case the initial nutrients controlled the dates of nutrient limitation and zero or negative net growth (Figure 10d).

4. Discussion

4.1. An Extensive, Long-Duration Ice Algae Bloom

The presence of ice algae at both buoy sites was indicated by the high light attenuation values through the ice, and the associated reduction of blue light in the under-ice light field caused by the presence of Chl *a* containing material. The SKs provided corroborating evidence via images of clumped algae at the sea surface. The gradual increase in $K_d PAR_{ICE}$ over time reveals the seasonal evolution of ice algae growth both within and attached to the bottom of the ice, a type of observation that has never been made before using autonomous sensor platforms.

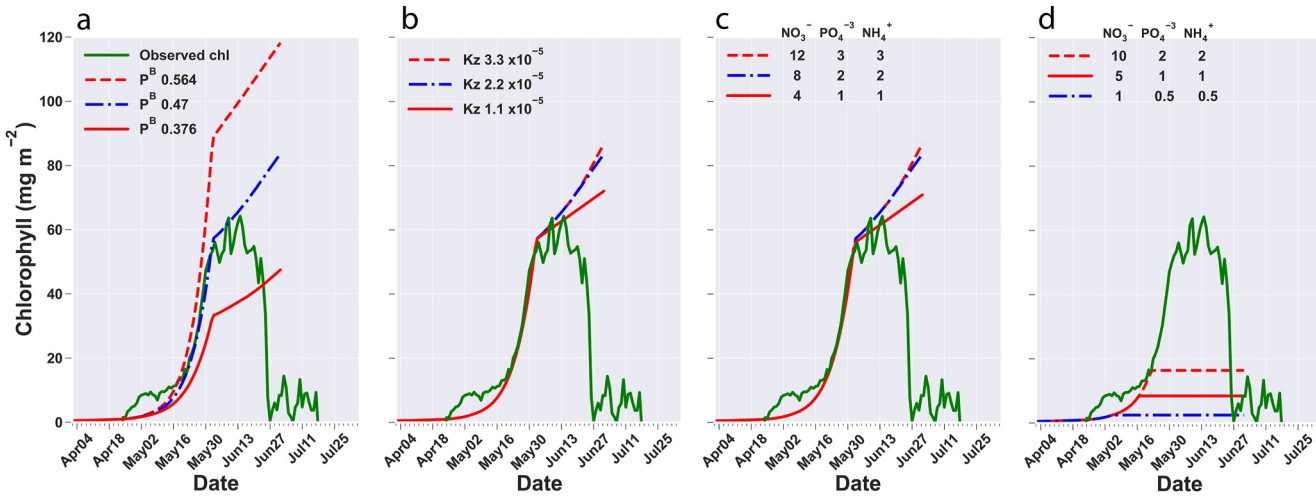

Figure 10. Sensitivity of ice algae productivity model to WB8 input variables. Model Chl *a* is overlaid on Chl *a* (green) from Figure 8. (a) biomass-specific photosynthesis rate (mg C mg Chl a^{-1} hr^{-1}), (b) Kz vertical eddy diffusivity (m^2 sec^{-1}), (c) nutrient pool concentration (mmol m^{-3}), (d) vertical diffusion off with variable initial nutrient concentration.

The main difference between the buoy sites was the influx of snow the week after deployment at the high snow site, leading to delayed ice algae growth. At the low snow site, ice algae growth started in April, Chl *a* reached ~10 mg m^{-2} by 26 April and 150 mg m^{-2} by the end of May. In contrast, reduced light transmission to the bottom of the ice at the high snow site delayed ice algae growth by approximately 3 weeks, and Chl *a* did not reach 10 mg m^{-2} until mid-May and ~50 mg m^{-2} at the end of May. As a historical comparison, ice algae Chl *a* measured in situ in the spring of 2002 by Gradinger (2009) in the same area of the Chukchi Sea was ~10 mg m^{-2} on 30 May. While we cannot determine the onset of algae growth with any certainly in 2002, it is apparent that the bloom phase of ice algal growth was reached far earlier at the low snow site in 2018. Ice algae was present for 63 days at the low snow site and only half of that (35 days) at the high snow site. Ice algae bloom duration is highly variable temporally and spatially across the Arctic. Blooms extending over 30–50 days have been observed primarily from landfast ice (Leu et al., 2015; Oziel et al., 2019). Unfortunately, there are no previous observations following the full growth and decline of sea ice algae in drifting pack ice, so the true length of ice algae blooms in seasonal ice is an unknown. However, modeling indicates that ice algae should respond to the changes in light availability by shifting phenology, increasing GPP and expanding their habitat to include the larger extent of seasonal ice (Horvat et al., 2017; Lannuzel et al., 2020; Tedesco et al., 2019). The early and persistent bloom observed at the low snow site suggests that this is already happening on the Chukchi shelf, with the caveat that snow thickness seems to be the driving factor here, and so these impacts are expected to be quite spatially heterogenous. We hypothesize that our observations at the low snow site may represent future conditions in the pack ice on the northern Chukchi Sea.

Since our observations are a time series taken at a single under-ice point and self-shading is likely (based on the density of algae present), these estimates represent a lower limit on total areal Chl *a*. Given that both buoys observed vigorous ice algae growth, we hypothesize that this situation existed over a large area of the northern Chukchi shelf. Our observations of the in-ice bloom ended prematurely when melting of the ice caused the uppermost sensors to drop out of the bottom of the ice and thus out of the bloom. Ice algae could have persisted for longer than observed from the buoy; however, the ice was breaking up at this time, naturally leading to the end of the bloom.

By reducing transmission to the upper ocean to ~1% of incident light, it is possible that ice algae at both sites may have had an inhibitory effect on water column photosynthesis. Although light transmission through the ice increased as the surface melted, the energy was absorbed by the ice algae and not available to fuel pelagic phytoplankton growth. Ice algae accounted for >90% of total Chl *a* (ice plus upper water column) through May, June and July, with continued low water column Chl *a* once the marginal ice zone moved northward. In past years, pelagic blooms have been observed in the Northern Chukchi Sea, reaching 30 mg m^{-3} in the upper water column (Arrigo et al., 2014; Hill et al., 2018) but our buoys detected none in 2018. Due to the relative motion

between ice and underlying water, the water column that the buoys observed was not tightly coupled to the light field's temporal history measured through the ice around the buoy site. Therefore, our buoy observations, while suggestive, cannot be used to definitively state that robust ice algae blooms were the primary cause of low water column productivity. However, satellite estimates of open water Chl *a* on the northern Chukchi shelf in June 2018 after ice retreat found lower values than the long-term average (Frey, 2018). Thus, we propose that GPP on the Northern Chukchi shelf in the spring and early summer of 2018 was dominated by ice algae, which potentially impacted water column primary production.

4.2. Light Versus Nutrient Limitation

Model results indicate that algal growth at the low snow site was light limited until approximately 30 April, after which nutrients became the limiting resource. Nutrient replenishment into the ice algae layer was represented by a vertical diffusivity term K_z equal to 1.6×10^{-5} (WB7) and 2.2×10^{-5} m^2 s^{-1} (WB8). These values are higher than previously used by Arrigo & Sullivan, 1994) to model nutrient-replete ice algae growth in McMurdo Sound, but lower than that observed under landfast ice in the Canadian Archipelago (Cota et al., 1987; Lavoie et al., 2005). At the height of the modeled ice algae growth at the low snow site, the nutrient demand was 3 mmol m^{-2} d^{-1} which is also greater than fluxes measured in situ under landfast ice in the Barrow Strait (Cota et al., 1987) and the Barents Sea (Bourgault et al., 2011, 2 mmol m^{-2} day^{-1}). We hypothesize that the ice algae bloom at the low snow site was supplied with nutrients through a combination of turbulence generated by ice-ocean stress and/or brine convection eroding the subsurface nutricline and mixing nutrients up to the base of the ice (Skyllingstad & Denbo, 2001) plus movement of the buoy into nutrient-rich water masses. At the time of the ice algae bloom (May–June), most of the northern Chukchi shelf was still ice-covered, and there was no indication of a water column bloom. Therefore, nutrients were likely to be replete, providing a constant new source of nutrients along the drift path of the buoys. With light limitation removed, initial nutrient concentrations in the ice and underlying water column, plus replenishment fluxes during the ice algae bloom became the limiting factor in ice algae GPP at the low snow site.

5. Conclusions

These data represent unique observations of the seasonal development of ice algae on first-year drifting sea ice. The presence of a dense bloom initialized earlier than has previously been observed for the Chukchi shelf provides evidence that predicted shifts in ice algae phenology have been initiated. Ice algae could be increasing, owing to an extensive seasonal ice area with thin snow cover that provides habitat and a longer window of growth. However, as the Arctic warms, the window for this growth could shorten as earlier light availability is counterbalanced by earlier ice melt. Nutrient flux into an ice algae layer in mobile seasonal ice is currently an unknown, and contributes a large uncertainty in our ability to predict future ice algae GPP. As climate modeling indicates that ice algae GPP will be proportional to nutrient availability (Tedesco et al., 2019), determining present and future nutrient dynamics via both upper ocean stratification and biogeochemical processes in brine channels is critical to projecting the full impact of Arctic change on ice algae (Lannuzel et al., 2020).

6. Considerations for Future Work

With thinner ice and thinner snow cover predicted to become the new normal for much of the Arctic ice pack, nutrient availability will be the dominant factor in limiting ice algae GPP. Incorporating nutrient measurements into the WARM buoys could help identify the mechanisms responsible for nutrient replenishment into the ice algae layer, critical for future predictions of both ice algae and pelagic phytoplankton production. The design of cheaper sensors and the inclusion of WARM buoy deployments in larger projects could reduce the cost for any single investigator, and increase annual deployment which to date has been limited by cost. Future deployments should coordinate WARM buoys with instrument clusters such as ice mass-balance buoys that provide complementary data on snow and ice accumulation and ablation. Combining WARM buoy data with water column observations from moorings, Argo floats, and ROVs (Randelhoff et al., 2020) and the inclusion of targeted high-resolution satellite remote sensing (sub 30 m; Wright & Polashenski, 2018) can provide a broader spatial scale for ice-tethered measurements.

Conflict of Interest

The authors declare no conflicts of interest relevant to this study.

Data Availability Statement

The observational data collected by the buoys are available at NSF Arctic Data Center via https://doi.org/10.18739/A2Z31NP9F (Hill et al., 2020).

Acknowledgments
This study was funded by NSF Office of Polar Programs through grants AON 1603548 (V. Hill) and PLR-1602521 (B. Light and M. Steele). Our thanks to the staff at UIC Science LLC in Utqiaġvik and Polar Field Services for logistics support.

References

Ardyna, M., Mundy, C. J., Mayot, N., Matthes, L. C., Oziel, L., Horvat, C., et al. (2020). Under-ice phytoplankton blooms: Shedding light on the "invisible" part of Arctic primary production. *Frontiers in Marine Science*, *7*(985). https://doi.org/10.3389/fmars.2020.608032

Arndt, S., & Nicolaus, M. (2014). Seasonal cycle and long-term trend of solar energy fluxes through Arctic sea ice. *The Cryosphere*, *8*(6), 2219–2233. https://doi.org/10.5194/tc-8-2219-2014

Arrigo, K. R., Perovich, D. K., Pickart, R. S., Brown, Z. W., Van Dijken, G. L., Lowry, K. E., et al. (2012). Massive phytoplankton blooms under Arctic sea ice. *Science*, *336*, 1408. https://doi.org/10.1126/science.1215065

Arrigo, K. R., Perovich, D. K., Pickart, R. S., Brown, Z. W., Van Dijken, G. L., Lowry, K. E., et al. (2014). Phytoplankton blooms beneath the sea ice in the Chukchi sea. *Deep-Sea Research Part Ii-Topical Studies in Oceanography*, *105*, 1–16. https://doi.org/10.1016/j.dsr2.2014.03.018

Arrigo, K. R., & Sullivan, C. W. (1994). A high resolution bio-optical model of microalgal growth: Tests using sea-ice algal community time-series data. *Limnology & Oceanography*, *39*(3), 609–631. https://doi.org/10.4319/lo.1994.39.3.0609

Assmy, P., Fernandez-Mendez, M., Duarte, P., Meyer, A., Randelhoff, A., Mundy, C. J., et al. (2017). Leads in Arctic pack ice enable early phytoplankton blooms below snow-covered sea ice. *Scientific Reports*, *7*. https://doi.org/10.1038/srep40850

Balch, W. M., Bowler, B. C., Lubelczyk, L. C., & Stevens, M. W. (2014). Aerial extent, composition, bio-optics and biogeochemistry of a massive under-ice algal bloom in the Arctic. *Deep-Sea Research Part Ii-Topical Studies in Oceanography*, *105*, 42–58. https://doi.org/10.1016/j.dsr2.2014.04.001

Boetius, A., Albrecht, S., Bakker, K., Bienhold, C., Felden, J., Fernández-Méndez, M., et al. (2013). Export of algal biomass from the melting Arctic sea ice. *Science*, *339*(6126), 1430–1432. https://doi.org/10.1126/science.1231346

Bourgault, D., Hamel, C., Cyr, F., Tremblay, J. É., Galbraith, P., Dumont, D., & Gratton, Y. (2011). Turbulent nitrate fluxes in the Amundsen Gulf during ice-covered conditions. *Geophysical Research Letters*, *38*(15). https://doi.org/10.1029/2011gl047936

Castellani, G., Schaafsma, F. L., Arndt, S., Lange, B. A., Peeken, I., Ehrlich, J., et al. (2020). Large-scale variability of physical and biological sea-ice properties in polar oceans. *Frontiers in Marine Science*, *536*. https://doi.org/10.3389/fmars.2020.00536

Codispoti, L. A., Kelly, V., Thessen, A., Matrai, P., Suttles, S., Hill, V., et al. (2013). Synthesis of primary production in the Arctic Ocean: III. Nitrate and phosphate based estimates of net community production. *Progress in Oceanography*, *110*, 126–150. https://doi.org/10.1016/j.pocean.2012.11.006

Cota, G. F. (1985). Photoadaptation of high Arctic ice algae. *Nature*, *315*(6016), 219–222. https://doi.org/10.1038/315219a0

Cota, G. F., Prinsenberg, S. J., Benett, E. B., Loder, J. W., Lewis, M. R., Anning, J. L., et al. (1987). Nutrient fluxes during extended blooms of Arctic ice algae. *Journal of Geophysical Research*, *92*(C2), 1951–1962. https://doi.org/10.1029/jc092ic02p01951

Dou, T., Xiao, C., Liu, J., Han, W., Du, Z., Mahoney, A. R., et al. (2019). A key factor initiating surface ablation of Arctic sea ice: Earlier and increasing liquid precipitation. *The Cryosphere*, *13*(4), 1233–1246. https://doi.org/10.5194/tc-13-1233-2019

Ehn, J. K., & Mundy, C. J. (2013). Assessment of light absorption within highly scattering bottom sea ice from under-ice light measurements: Implications for Arctic ice algae primary production. *Limnology & Oceanography*, *58*(3), 893–902. https://doi.org/10.4319/lo.2013.58.3.0893

Emerson, R., & Lewis, C. M. (1943). The dependence of the quantum yield of chlorella photosynthesis on wave length of light. *American Journal of Botany*, *30*(3), 165–178. https://doi.org/10.1002/j.1537-2197.1943.tb14744.x

Feng, Z., Ji, R., Ashjian, C., Zhang, J., Campbell, R., & Grebmeier, J. M. (2021). Benthic hotspots on the northern Bering and Chukchi continental shelf: Spatial variability in production regimes and environmental drivers. *Progress in Oceanography*, *191*, 102497. https://doi.org/10.1016/j.pocean.2020.102497

Forest, A., Tremblay, J. E., Gratton, Y., Martin, J., Gagnon, J., Darnis, G., et al. (2011). Biogenic carbon flows through the planktonic food web of the Amundsen Gulf (Arctic ocean): A synthesis of field measurements and inverse modeling analyses. *Progress in Oceanography*, *91*(4), 410–436. https://doi.org/10.1016/j.pocean.2011.05.002

Frey, K. (2018). Arctic Ocean primary productivity: The response of marine algae to climate warming and sea ice decline. *Arctic Report Card 2018*. https://www.arctic.noaa.gov/Report-Card/Report-Card-2018/ArtMID/7878/ArticleID/778/Arctic-Ocean-Primary-Productivity-The-Response-of-Marine-Algae-to-Climate-Warming-and-Sea-Ice-Decline

Gosselin, M., Legendre, L., Therriault, J.-C., Demers, S., & Rochet, M. (1986). Physical control of the horizontal patchiness of sea-ice microalgae. *Marine Ecology Progress Series*, *29*(3), 289–298. https://doi.org/10.3354/meps029289

Gradinger, R. (2009). Sea-ice algae: Major contributors to primary production and algal biomass in the Chukchi and Beaufort Seas during May/June 2002. *Deep-Sea Research Part Ii-Topical Studies in Oceanography*, *56*(17), 1201–1212. https://doi.org/10.1016/j.dsr2.2008.10.016

Hancke, K., Lund-Hansen, L. C., Lamare, M. L., Højlund Pedersen, S., King, M. D., Andersen, P., & Sorrell, B. K. (2018). Extreme low light requirement for algae growth underneath sea ice: A case study from station Nord, NE Greenland. *Journal of Geophysical Research: Oceans*, *123*(2), 985–1000. https://doi.org/10.1002/2017jc013263

Hill, V. (2004). *The Western Arctic Shelf-Basin Interactions (SBI) experiment contains measurements made in the Chukchi and Beaufort seas off the coast of northern Alaska*. NASA SeaBASS. https://doi.org/10.5067/SeaBASS/SBI/DATA001

Hill, V., Light, B., & Steele, M. (2016). *Warming and irradiance measurements in the Arctic: Determining the link between solar energy absorption and surface warming through long term observations*. Arctic Data Center, NSF Arctic Data Center. https://doi.org/10.18739/A2G73748M

Hill, V., Light, B., & Steele, M. (2020). Warming and irradiance measurement (WARM) buoys deployed in Canada basin and Chukchi shelf Arctic ocean. *Arctic Data Center*. https://doi.org/10.18739/A2Z31NP9F

Hill, V. J., Light, B., Steele, M., & Zimmerman, R. C. (2018). Light availability and phytoplankton growth beneath Arctic Sea Ice: Integrating observations and modeling. *Journal of Geophysical Research-Oceans*, *123*(5), 3651–3667. https://doi.org/10.1029/2017jc013617

Horvat, C., Jones, D. R., Iams, S., Schroeder, D., Flocco, D., & Feltham, D. (2017). The frequency and extent of sub-ice phytoplankton blooms in the Arctic Ocean. *Science Advances*, *3*(3). https://doi.org/10.1126/sciadv.1601191

Jin, M., Deal, C. J., Wang, J., Shin, K.-H., Tanaka, N., Whitledge, T. E., et al. (2006). Controls of the landfast ice–ocean ecosystem offshore Barrow, Alaska. *Annals of Glaciology*, *44*, 63–72. https://doi.org/10.3189/172756406781811709

Johnson, M., & Eicken, H. (2016). Estimating Arctic sea-ice freeze-up and break-up from the satellite record: A comparison of different approaches in the Chukchi and Beaufort seas. *Elementa: Science of Anthropocene*, *4*. https://doi.org/10.12952/journal.elementa.000124

Koch, C. W., Cooper, L. W., Lalande, C., Brown, T. A., Frey, K. E., & Grebmeier, J. M. (2020). Seasonal and latitudinal variations in sea ice algae deposition in the Northern Bering and Chukchi Seas determined by algal biomarkers. *PLoS One*, *15*(4), e0231178. https://doi.org/10.1371/journal.pone.0231178

Kwok, R. (2018). Arctic sea ice thickness, volume, and multiyear ice coverage: Losses and coupled variability (1958–2018). *Environmental Research Letters*, *13*(10), 105005. https://doi.org/10.1088/1748-9326/aae3ec

Laney, S. R., Krishfield, R. A., & Toole, J. M. (2017). The euphotic zone under Arctic Ocean sea ice: Vertical extents and seasonal trends. *Limnology & Oceanography*, *62*(5), 1910–1934. https://doi.org/10.1002/lno.10543

Lange, B. A., Katlein, C., Castellani, G., Fernández-Méndez, M., Nicolaus, M., Peeken, I., & Flores, H. (2017). Characterizing spatial variability of ice algal chlorophyll a and net primary production between sea ice habitats using horizontal profiling platforms. *Frontiers in Marine Science*, *4*, 349. https://doi.org/10.3389/fmars.2017.00349

Lannuzel, D., Tedesco, L., Van Leeuwe, M., Campbell, K., Flores, H., Delille, B., et al. (2020). The future of Arctic sea-ice biogeochemistry and ice-associated ecosystems. *Nature Climate Change*, *10*(11), 983–992. https://doi.org/10.1038/s41558-020-00940-4

Lavoie, D., Denman, K., & Michel, C. (2005). Modeling ice algal growth and decline in a seasonally ice-covered region of the Arctic (Resolute Passage, Canadian Archipelago). *Journal of Geophysical Research*, *110*(C11). https://doi.org/10.1029/2005jc002922

Laws, E. A. (1991). Photosynthetic quotients, new production and net community production in the Open Ocean. *Deep-Sea Research, Part A: Oceanographic Research Papers*, *38*(1), 143–167. https://doi.org/10.1016/0198-0149(91)90059-O

Leu, E., Mundy, C. J., Assmy, P., Campbell, K., Gabrielsen, T. M., Gosselin, M., et al. (2015). Arctic spring awakening - Steering principles behind the phenology of vernal ice algal blooms. *Progress in Oceanography*, *139*, 151–170. https://doi.org/10.1016/j.pocean.2015.07.012

Light, B., Perovich, D. K., Webster, M. A., Polashenski, C., & Dadic, R. (2015). Optical properties of melting first-year Arctic sea ice. *Journal of Geophysical Research-Oceans*, *120*(11), 7657–7675. https://doi.org/10.1002/2015jc011163

Light, B. T., Grenfell, T. C., & Perovich, D. K. (2008). Transmission and absorption of solar radiation by Arctic sea ice during the melt season. *Journal of Geophysical Research*, *113*(C3). https://doi.org/10.1029/2006JC003977

Lowry, K. E., Pickart, R. S., Mills, M. M., Brown, Z. W., Van Dijken, G. L., Bates, N. R., & Arrigo, K. R. (2015). The influence of winter water on phytoplankton blooms in the Chukchi Sea. *Deep-Sea Research Part Ii-Topical Studies in Oceanography*, *118*, 53–72. https://doi.org/10.1016/j.dsr2.2015.06.006

Lund-Hansen, L. C., Søgaard, D. H., Sorrell, B. K., Gradinger, R., & Meiners, K. M. (2020). Spring, summer and melting sea ice. In *Arctic sea ice ecology: Seasonal dynamics in algal and bacterial productivity* (pp. 61–101). Springer International Publishing. https://doi.org/10.1007/978-3-030-37472-3_4

McMinn, A., & Hegseth, E. N. (2004). Quantum yield and photosynthetic parameters of marine microalgae from the southern Arctic Ocean, Svalbard. *Journal of the Marine Biological Association of the United Kingdom*, *84*(5), 865–871. https://doi.org/10.1017/S0025315404010112h

Meiners, K., Arndt, S., Bestley, S., Krumpen, T., Ricker, R., Milnes, M., et al. (2017). Antarctic pack ice algal distribution: Floe-scale spatial variability and predictability from physical parameters. *Geophysical Research Letters*, *44*(14), 7382–7390. https://doi.org/10.1002/2017gl074346

Melbourne-Thomas, J., Meiners, K. M., Mundy, C., Schallenberg, C., Tattersall, K. L., & Dieckmann, G. S. (2015). Algorithms to estimate Antarctic sea ice algal biomass from under-ice irradiance spectra at regional scales. *Marine Ecology Progress Series*, *536*, 107–121. https://doi.org/10.3354/meps11396

Michel, C., Legendre, L., Ingram, R. G., Gosselin, M., & Levasseur, M. (1996). Carbon budget of sea-ice algae in spring: Evidence of a significant transfer to zooplankton grazers. *Journal of Geophysical Research*, *101*(C8), 18345–18360. https://doi.org/10.1029/96JC00045

Mock, T., & Gradinger, R. (1999). Determination of Arctic ice algal production with a new in situ incubation technique. *Marine Ecology Progress Series*, *177*, 15–26. https://doi.org/10.3354/meps177015

Mock, T., & Gradinger, R. (2000). Changes in photosynthetic carbon allocation in algal assemblages of Arctic sea ice with decreasing nutrient concentrations and irradiance. *Marine Ecology Progress Series*, *202*, 1–11. https://doi.org/10.3354/meps202001

Mortenson, E., Hayashida, H., Steiner, N., Monahan, A., Blais, M., Gale, M. A., et al. (2017). A model-based analysis of physical and biological controls on ice algal and pelagic primary production in Resolute Passage. *Elementa: Science of the Anthropocene*, *5*. https://doi.org/10.1525/elementa.229

Mundy, C.-J., Ehn, J. K., Barber, D., & Michel, C. (2007). Influence of snow cover and algae on the spectral dependence of transmitted irradiance through Arctic landfast sea ice. *Journal of Geophysical Research*, *112*. https://doi.org/10.1029/2006jc003683

Mundy, C. J., Gosselin, M., Gratton, Y., Brown, K., Galindo, V., Campbell, K., et al. (2014). Role of environmental factors on phytoplankton bloom initiation under landfast sea ice in Resolute Passage, Canada. *Marine Ecology Progress Series*, *497*, 39–49. https://doi.org/10.3354/meps10587

Nicolaus, M., Katlein, C., Maslanik, J., & Hendricks, S. (2012). Changes in Arctic sea ice result in increasing light transmittance and absorption. *Geophysical Research Letters*, *39*(24). https://doi.org/10.1029/2012gl053738

Oziel, L., Massicotte, P., Randelhoff, A., Ferland, J., Vladoiu, A., Lacour, L., et al. (2019). Environmental factors influencing the seasonal dynamics of spring algal blooms in and beneath sea ice in Western Baffin Bay, Elementa. *Science of the Anthropocene*, *7*. https://doi.org/10.1525/elementa.372

Perovich, D., Meier, W., Tschudi, M., Farrell, S., Hendricks, S., Gerland, S., et al. (2019). Sea ice. In J. A. Richter-Menge, M. L. Druckenmiller, & M. Jefferies (Eds.), *Arctic report card 2019*. Retrieved from https://www.arctic.noaa.gov/Report-Card

Perovich, D. K., & Polashenski, C. (2012). Albedo evolution of seasonal Arctic sea ice. *Geophysical Research Letters*, *39*. https://doi.org/10.1029/2012gl051432

Platt, T., Gallegos, C., & Harrison, W. (1980). Photoinhibition of photosynthesis in natural assemblages of marine phytoplankton. *Journal of Marine Research*.

Platt, T., Harrison, W. G., Irwin, B., Horne, E. P., & Gallegos, C. L. (1982). Photosynthesis and photoadaptation of marine-phytoplankton in the Arctic. *Deep-Sea Research, Part A: Oceanographic Research Papers*, *29*(10), 1159–1170. https://doi.org/10.1016/0198-0149(82)90087-5

Polashenski, C., Perovich, D., & Courville, Z. (2012). The mechanisms of sea ice melt pond formation and evolution. *Journal of Geophysical Research-Oceans*, *117*. https://doi.org/10.1029/2011jc007231

Poulin, M., Daugbjerg, N., Gradinger, R., Ilyash, L., Ratkova, T., & Von Quillfeldt, C. (2011). The pan-Arctic biodiversity of marine pelagic and sea-ice unicellular eukaryotes: A first-attempt assessment. *Marine Biodiversity*, *41*(1), 13–28. https://doi.org/10.1007/s12526-010-0058-8

Randelhoff, A., Lacour, L., Marec, C., Leymarie, E., Lagunas, J., Xing, X., et al. (2020). Arctic mid-winter phytoplankton growth revealed by autonomous profilers. *Science Advances*, *6*(39). https://doi.org/10.1126/sciadv.abc2678

Richter-Menge, J. A., & Druckenmiller, M. L. (2020). The Arctic [in "state of the climate 2019']. *Bulletin of American Meterorological Society*, *101*(8), S239–S285. https://doi.org/10.1175/BAMS-D-20-0086.1

Skyllingstad, E. D., & Denbo, D. W. (2001). Turbulence beneath sea ice and leads: A coupled sea ice/large-eddy simulation study. *Journal of Geophysical Research*, *106*(C2), 2477–2497. https://doi.org/10.1029/1999jc000091

Stroeve, J., & Notz, D. (2018). Changing state of Arctic sea ice across all seasons. *Environmental Research Letters*, *13*(10), 103001. https://doi.org/10.1088/1748-9326/aade56

Syvertsen, E. E. (1991). Ice algae in the Barents Sea: Types of assemblages, origin, fate and role in the ice-edge phytoplankton bloom. *Polar Research*, *10*(1), 277–288. https://doi.org/10.3402/polar.v10i1.6746

Tedesco, L., Vichi, M., & Scoccimarro, E. (2019). Sea-ice algal phenology in a warmer Arctic. *Science Advances*, *5*(5). https://doi.org/10.1126/sciadv.aav4830

Thomas, D. N., Papadimitriou, S., & Michel, C. (2010). In D. N. Thomas & G. S. Dieckmann (Eds.), *Biogeochemistry of sea ice in sea ice* (pp. 425–468). Wiley-Blackwell.

Vancoppenolle, M., Goosse, H., De Montety, A., Fichefet, T., Tremblay, B., & Tison, J. L. (2010). Modeling brine and nutrient dynamics in Antarctic sea ice: The case of dissolved silica. *Journal of Geophysical Research: Oceans*, *115*. https://doi.org/10.1029/2009jc005369

Wang, J., Cota, G. F., & Ruble, D. A. (2005). Absorption and backscattering in the Beaufort and Chukchi Seas Chukchi Sea. *Journal of Geophysical Research*, *110*(C04014). https://doi.org/10.1029/2002JC001653

Webster, M., Gerland, S., Holland, M., Hunke, E., Kwok, R., Lecomte, O., et al. (2018). Snow in the changing sea-ice systems. *Nature Climate Change*, *8*(11), 946–953. https://doi.org/10.1038/s41558-018-0286-7

Welch, H. E., & Bergmann, M. A. (1989). Seasonal development of ice algae and its prediction from environmental factors near Resolute, NWT, Canada. *Canadian Journal of Fisheries and Aquatic Sciences*, *46*(10), 1793–1804. https://doi.org/10.1139/f89-227

Wright, N. C., & Polashenski, C. M. (2018). Open-source algorithm for detecting sea ice surface features in high-resolution optical imagery. *The Cryosphere*, *12*(4), 1307–1329. https://doi.org/10.5194/tc-12-1307-2018

Zeebe, R. E., Eicken, H., Robinson, D. H., Wolf-Gladrow, D., & Dieckmann, G. S. (1996). Modeling the heating and melting of sea ice through light absorption by microalgae. *Journal of Geophysical Research*, *101*(C1), 1163–1181. https://doi.org/10.1029/95jc02687